clean technologies

Article

Deciphering Temperature–Humidity Coupling in Proton Exchange Membrane Fuel Cells: Multiphysics Insights into Performance, Water Management, and Operating Limits

Akram E. Zeid [1], Saad S. Alrwashdeh [1,2,*], Mohammad R. Almajali [3], Ahmed M. Salem [1] and Nathan Kawansson [4]

[1] Marine Engineering Technology, Sharjah Maritime Academy, Sharjah P.O. Box 180018, United Arab Emirates
[2] Mechanical Engineering Department, Faculty of Engineering, Mutah University, Al-Karak 61710, Jordan
[3] Defence and Security Program, Rabdan Academy, Abu Dhabi P.O. Box 114646, United Arab Emirates
[4] Maritime Logistics and Supply Chain Management (MLSCM), Sharjah Maritime Academy, Sharjah P.O. Box 180018, United Arab Emirates
* Correspondence: saad.alrwashdeh@sma.ac.ae

Abstract

Climate-driven temperature and humidity extremes can substantially alter the coupled electrochemical, thermal, and transport processes governing proton exchange membrane fuel cell (PEMFC) performance, yet their implications for environmental resilience remain insufficiently quantified. This study develops a three-dimensional, non-isothermal multiphysics framework to assess PEMFC operation across 16 temperature–relative-humidity scenarios spanning 20–80 °C and 20–100% RH. Electrochemical kinetics, species and heat transport, membrane hydration, liquid-water behavior, oxygen availability, and spatial current-density characteristics are evaluated concurrently to identify environmentally induced operating limitations. The results reveal two competing failure regimes: hot–dry exposure promotes membrane dehydration, increased protonic resistance, spatial non-uniformity, and severe power deterioration, whereas excessive humidification progressively increases liquid-water accumulation, oxygen-transport resistance, pressure drop, and auxiliary pumping requirements. A balanced regime emerges around 60 °C and 80% RH (C11), where membrane hydration and oxygen accessibility are simultaneously maintained. Under this condition, oxygen utilization reaches approximately 79.4%, the admissible current density increases to 1.98 A cm^{-2}, and net power density reaches approximately 1.04 W cm^{-2}. In contrast, the hot–dry C13 condition restricts the admissible current density to 0.74 A cm^{-2} and reduces net power density to approximately 0.49 W cm^{-2}. The findings demonstrate that PEMFC climate resilience is governed by the balance between hydration preservation and reactant/water transport rather than optimization of temperature or humidity independently, providing a physics-based basis for climate-adaptive control and robust hydrogen-power-system design.

Keywords: proton exchange membrane fuel cell; environmental resilience; climate extremes; multiphysics modeling; hydrogen power systems

Academic Editor: Damien Guilbert

Received: 15 October 2026
Revised: 9 November 2026
Accepted: 12 November 2026
Published: 16 November 2026

Copyright: © 2026 by the authors. Licensee MDPI, Basel, Switzerland. This article is an open access article distributed under the terms and conditions of the Creative Commons Attribution (CC BY) license.

1. Introduction

The global transition toward low-carbon and climate-neutral energy systems has intensified interest in hydrogen as a versatile energy carrier capable of supporting the decarbonization of transportation, distributed power generation, maritime applications, and energy-intensive industrial sectors. When hydrogen is produced using low-carbon or renewable electricity, proton exchange membrane fuel cells (PEMFCs) provide an attractive pathway for converting its chemical energy directly into electricity with high efficiency, rapid start-up, low operating temperature, high power density, and zero carbon emissions at the point of use. These characteristics have positioned PEMFC technology among the leading electrochemical conversion systems for future sustainable hydrogen infrastructures. Nevertheless, widespread deployment requires not only improvements in efficiency and durability but also reliable operation under environmental conditions that may vary substantially across geographical locations and seasons. In this context, the resilience of PEMFC systems to environmental stresses is becoming increasingly important as climate change contributes to more frequent and severe temperature and humidity extremes [1–4].

PEMFC operation involves strongly coupled electrochemical, thermal, fluid-dynamic, and mass-transport phenomena occurring simultaneously within relatively thin and heterogeneous porous layers. Hydrogen oxidation at the anode supplies protons that migrate through the polymer electrolyte membrane, while electrons travel through the external circuit before participating in the oxygen reduction reaction at the cathode. Water and heat are generated as reaction products, creating complex interactions between local temperature, membrane hydration, vapor transport, liquid-water formation, gas diffusion, and electrochemical reaction rates. Consequently, changes in environmental or operating conditions can propagate through several physical mechanisms rather than affecting a single performance parameter [5–11]. Temperature and relative humidity are particularly influential because they simultaneously govern reaction kinetics, saturation pressure, membrane water content, proton conductivity, evaporation and condensation, and the transport of reactant species through the gas diffusion and catalyst layers.

Effective water management represents one of the fundamental challenges in achieving stable PEMFC operation. The polymer electrolyte membrane must retain sufficient water to maintain high proton conductivity, yet excessive water accumulation within the cathode catalyst layer, gas diffusion layer, or flow channels can restrict oxygen transport and cause flooding. Under dry conditions, insufficient membrane hydration increases ionic resistance and associated ohmic losses, potentially producing substantial reductions in voltage and power output. Conversely, excessively humid conditions can promote condensation and liquid-water accumulation, particularly at high current densities where electrochemically generated water becomes significant [12–14]. The optimum operating state therefore exists within a relatively narrow balance between membrane hydration and effective removal of excess water. Importantly, this balance is temperature dependent because increasing temperature changes water saturation pressure, evaporation rates, membrane hydration characteristics, and electrochemical kinetics simultaneously. Experimental studies have accordingly demonstrated strong interactions between reactant humidification and operating temperature rather than completely independent effects of these variables [15–17].

Temperature introduces an equally complex trade-off. Moderate increases in operating temperature can accelerate electrochemical kinetics, improve catalyst activity, enhance gas-phase transport, and facilitate the evaporation and removal of excess liquid water. However, these advantages may diminish or even reverse when increased temperature is combined with insufficient humidity. Under hot and dry conditions, accelerated evaporation can reduce membrane water content and proton conductivity,

https://doi.org/10.3390/cleantechnol8060188

increase ohmic resistance and generate spatially non-uniform electrochemical activity. At the opposite extreme, lower temperatures reduce saturation pressure and favor condensation, thereby increasing the possibility of water accumulation and oxygen-transport limitations. Such behavior indicates that temperature cannot be considered independently from humidity when evaluating PEMFC performance [18–22]. More importantly, environmental extremes may create competing degradation mechanisms in which dehydration dominates one operating region while flooding and mass-transfer limitations dominate another. This coupled behavior becomes especially relevant when PEMFC systems are expected to operate reliably outside tightly controlled laboratory environments [15,23–25].

Several researchers have investigated these thermal and humidity effects from experimental, numerical, and system-level perspectives. Hottinen et al. experimentally examined a free-breathing PEMFC under controlled ambient temperature and relative humidity and demonstrated substantial changes in cell performance and current distribution as environmental conditions varied [26]. Kim and Hong investigated humidity and operating-temperature effects on PEMFC stacks, while Coppo et al. emphasized the role of operating temperature in controlling liquid-water transport and removal within the gas diffusion layer [27]. Saleh et al. investigated symmetrical and asymmetrical humidification conditions at different temperatures, demonstrating the importance of coupled humidity-temperature behavior [28]. These and other investigations were synthesized in the work reported in several studies, highlighting temperature and reactant humidification as major operating parameters controlling PEMFC performance. More recently, Lim et al. developed a sensor-integrated PEMFC capable of spatially resolving temperature, relative humidity, and pressure and demonstrated direct correlations between internal environmental distributions, water transport, and electrochemical performance. Collectively, these investigations establish the fundamental sensitivity of PEMFCs to thermal and moisture conditions but also indicate the need for integrated assessment across broader combinations of environmental extremes [29,30].

The importance of this problem becomes more pronounced when PEMFCs are considered for operation in regions characterized by severe or highly variable climates. Hot and arid environments, for example, combine elevated ambient temperatures with low relative humidity, creating particularly unfavorable conditions for maintaining membrane hydration. A three-dimensional investigation using annual climatic conditions from Abu Dhabi demonstrated that open-cathode PEMFC stack performance could vary substantially between winter and summer, with hot and dry conditions producing membrane dehydration and significant deterioration in performance; humidification was shown to recover a considerable portion of the lost performance. At the other environmental extreme, high-humidity conditions can reduce dehydration risk but intensify water-management requirements and increase susceptibility to flooding. Recent experimental work on open-cathode systems has further confirmed measurable sensitivity of stack power and efficiency to combinations of ambient temperature and relative humidity. These observations suggest that future PEMFC deployment should increasingly consider not simply nominal operating conditions but the ability of the system to tolerate and recover from environmental extremes [31–33].

Despite extensive research on PEMFC thermal and water management, much of the available literature evaluates temperature or relative humidity through conventional parametric studies focused primarily on polarization behavior, efficiency, or individual transport mechanisms. Comparatively less attention has been directed toward interpreting their coupled effects from the perspective of environmental resilience under climate change. This distinction is important because climate resilience requires

identifying not only conditions that maximize performance but also the boundaries beyond which stable operation becomes compromised and the physical mechanisms responsible for those transitions. Furthermore, cell voltage or power density alone may not adequately describe such behavior. Spatial distributions of membrane water content, temperature, oxygen concentration, current density, liquid-water saturation, and associated transport losses are necessary to distinguish dehydration-dominated operation from flooding-dominated regimes and to identify potentially resilient operating windows. A multiphysics approach is particularly suitable for this purpose because it can resolve the interactions among electrochemical reactions, heat generation and transfer, multiphase water behavior, species transport, and membrane proton conduction [4,7,20,21,23,34–36].

Accordingly, a significant research opportunity exists to establish a systematic relationship between environmental temperature–humidity extremes and the internal multiphysics response of PEMFCs. Such an approach should move beyond identifying whether increasing temperature or humidity improves or reduces overall performance and instead determine why, where, and under which combinations performance deterioration occurs. Mapping these interactions can reveal critical thresholds, synergistic stresses, and compensating effects that may remain hidden in conventional single-parameter analyses. It can also provide a foundation for defining temperature–humidity resilience maps and identifying operating envelopes within which acceptable electrochemical performance, membrane hydration, reactant accessibility, and thermal stability can simultaneously be maintained. Such information is relevant to the development of adaptive humidification, cooling, flow-management, and control strategies for PEMFC systems intended for transportation, stationary, maritime, and other hydrogen-powered applications exposed to increasingly variable climatic conditions [15,16,25,37–39].

Although the individual effects of temperature and relative humidity on PEMFC polarization characteristics, membrane conductivity, and water management have been extensively investigated, the present study extends these established relationships by examining their coupled influence on multiple interacting physical mechanisms within a consistent three-dimensional multiphysics framework. The contribution lies in connecting environmental stress conditions with the simultaneous evolution of electrochemical losses, membrane hydration, oxygen transport, liquid-water accumulation, thermal nonuniformity, and spatial current-density distributions, rather than evaluating polarization characteristics alone. The systematic comparison of 16 temperature–humidity scenarios enable the identification of dehydration-dominated, balanced, and flooding-prone operating regimes and provides a quantitative basis for comparing their relative environmental tolerance. These findings offer mechanistic insights into the operating limitations associated with coupled thermal and humidity stresses. Nevertheless, the framework is not intended to represent an exhaustive assessment of commercial PEMFC operation, and its applicability to automotive and stationary systems requires further validation under realistic operating profiles, transient environmental variations, and system-specific thermal and water-management conditions.

In this work, the environmental resilience of a PEM fuel cell under temperature and relative-humidity extremes is investigated using a coupled multiphysics modeling framework. The study systematically examines the interaction between thermal conditions and humidity levels and their influence on electrochemical performance, heat and mass transport, membrane hydration, oxygen availability, water behavior, and spatial current-density characteristics. Rather than treating temperature and humidity as isolated operating variables, different combinations are evaluated to identify the mechanisms governing dehydration, balanced water management, and flooding-

dominated operation. Attention is directed toward establishing the transition between these regimes and determining the environmental operating window within which stable and efficient PEMFC performance can be sustained. The resulting analysis is intended to establish a physics-based framework for assessing PEMFC resilience under climate-relevant environmental stresses and to provide guidance for adaptive thermal and water-management strategies for sustainable hydrogen power systems.

2. Multiphysics Modeling Framework and Environmental Stress Scenarios

A three-dimensional, steady-state, non-isothermal multiphysics model was developed to investigate the environmental resilience of a proton exchange membrane fuel cell (PEMFC) exposed to coupled temperature and relative-humidity extremes. The computational framework simultaneously considers fluid flow, species transport, electrochemical reactions, electronic and protonic charge transport, heat transfer, membrane hydration, and water transport. Attention is given to the interaction between temperature and relative humidity because these environmental parameters directly influence membrane water content, proton conductivity, electrochemical kinetics, oxygen transport, vapor saturation, evaporation, condensation, and liquid-water accumulation. The integrated framework therefore enables the PEMFC response to environmental stresses to be evaluated from both overall performance and internal transport perspectives.

Steady-state conditions were adopted to isolate the influence of environmental temperature and humidity from transient start-up and shutdown effects. Hydrogen and air were supplied to the anode and cathode, respectively. The gaseous species were considered ideal mixtures, and the flow within the channels was assumed to be laminar. The gas diffusion layers (GDLs) and catalyst layers (CLs) were modeled as homogeneous porous media. The polymer electrolyte membrane was considered impermeable to electrons but conductive to protons, with its ionic conductivity dependent on both temperature and membrane water content. These assumptions provide an appropriate balance between computational complexity and the physical resolution required to examine environmental resilience [40–44].

2.1. Pem Fuel Cell Geometry and Computational Domain

The computational domain consists of the anode flow channel, anode gas diffusion layer, anode catalyst layer, polymer electrolyte membrane, cathode catalyst layer, cathode gas diffusion layer, and cathode flow channel. A straight-channel configuration was adopted to provide a controlled geometry in which the effects of temperature and humidity can be distinguished from geometrical influences.

At the anode catalyst layer, hydrogen is oxidized according to

$$H_2 \rightarrow 2H^+ + 2e^- \quad (1)$$

The generated protons migrate through the hydrated polymer membrane toward the cathode, while electrons are transferred through the electrically conducting solid phase and external circuit. At the cathode catalyst layer, oxygen reacts with the transported protons and electrons:

$$\tfrac{1}{2}O_2 + 2H^+ + 2e^- \rightarrow H_2O \quad (2)$$

The overall electrochemical reaction is therefore

$$H_2 + \tfrac{1}{2}O_2 \rightarrow H_2O + \text{electrical energy} + \text{heat} \quad (3)$$

The geometrical configuration is maintained unchanged throughout all environmental scenarios. Consequently, the differences obtained among the investigated cases originate from the imposed temperature and humidity conditions rather than changes in cell architecture.

The values listed in Table 1 represent the baseline computational configuration. The same dimensions and material-domain definitions are maintained for all simulations to permit direct comparison among the different environmental conditions.

Table 1. Representative geometrical parameters of the PEMFC computational domain.

Parameter	Symbol	Value	Unit
Channel length	Lch	50	mm
Channel width	Wch	1.0	mm
Channel height	Hch	1.0	mm
Gas diffusion layer thickness	δGDL	0.30	mm
Catalyst layer thickness	δCL	0.010	mm
Membrane thickness	δmem	0.050	mm
GDL porosity	εGDL	0.70	–
CL porosity	εCL	0.40	–

The membrane–electrode assembly (MEA) considered in this study is represented through a numerical computational model rather than an experimentally fabricated component. The MEA comprises a Nafion-type polymer electrolyte membrane positioned between the anode and cathode catalyst layers, with adjacent gas diffusion layers. The membrane hydration and proton-conductivity characteristics are described using established constitutive relationships for Nafion-type materials, while the geometrical and porous-medium properties are specified according to the baseline computational parameters summarized in Table 1. Accordingly, the investigated MEA represents a modeled reference configuration rather than a specifically identified commercial MEA or an assembly physically manufactured in-house. This approach enables the effects of temperature and relative humidity on electrochemical performance, membrane hydration, and transport phenomena to be evaluated independently of variations in MEA manufacturing procedures.

The manufacturing route employed for membrane–electrode assemblies (MEAs), particularly catalyst-coated membrane (CCM) and catalyst-coated substrate (CCS) configurations, can significantly influence electrode microstructure and the resulting electrochemical and transport characteristics. Differences in catalyst-layer deposition, drying, compression, and interfacial bonding may modify pore-size distribution, porosity, tortuosity, catalyst–ionomer connectivity, and the contact resistance between adjacent MEA components. In CCM configurations, direct catalyst deposition onto the membrane can influence membrane–electrode interfacial contact and proton transport, whereas CCS fabrication may produce different pore connectivity and interfacial characteristics due to catalyst deposition onto the gas diffusion substrate. These manufacturing-dependent variations can affect oxygen accessibility, liquid-water removal, effective diffusivity, and local electrochemical reaction distributions. In the present numerical framework, the catalyst and gas diffusion layers are represented as homogeneous porous media with fixed baseline porosities of 0.40 and 0.70, respectively, as specified in Table 1. Consequently, manufacturing-induced variations in pore morphology and electrode architecture are not explicitly resolved, allowing the coupled effects of temperature and relative humidity to be examined under consistent structural conditions. Future investigations incorporating manufacturing-dependent pore-size distributions, tortuosity,

permeability, and interfacial resistance would enable a more comprehensive assessment of the interaction between MEA fabrication methods and environmental resilience.

The three-dimensional computational domain of the PEMFC is illustrated in Figure 1, showing the anode and cathode flow channels, gas diffusion layers (GDLs), catalyst layers (CLs), and polymer electrolyte membrane. The model incorporates the coupled transport of reactant gases, heat, water, and electrical charge across the different cell components. Hydrogen enters through the anode flow channel, while humidified air is supplied through the cathode flow channel. The three-dimensional representation identifies the computational regions and interfaces considered in the multiphysics analysis.

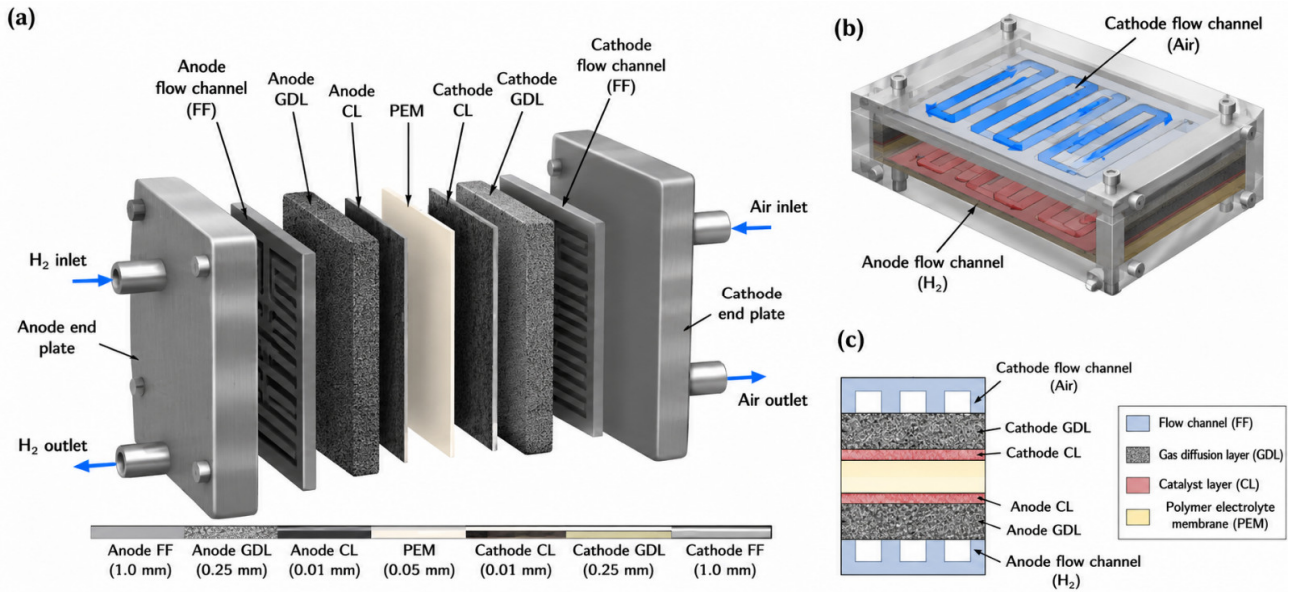


Figure 1. Three-dimensional schematic representation of the proton exchange membrane fuel cell (PEMFC) computational domain: (**a**) exploded view illustrating the anode and cathode flow channels, gas diffusion layers (GDLs), catalyst layers (CLs), and polymer electrolyte membrane (PEM); (**b**) assembled three-dimensional configuration showing the hydrogen and air flow pathways; and (**c**) cross-sectional view highlighting the arrangement of the individual cell components and their interfaces. The schematic illustrates the principal regions involved in the coupled electrochemical, fluid flow, heat transfer, and species transport processes.

2.2. Governing Multiphysics Transport and Electrochemical Model

The mathematical formulation is organized according to the principal physical processes governing PEMFC operation. Each governing equation is presented using consistent mathematical notation and is accompanied by definitions of the relevant variables and an explanation of its physical significance. The conservation equations describe the coupled transport of mass, momentum, chemical species, energy, and electrical charge, while the constitutive relationships establish the interactions among electrochemical kinetics, membrane hydration, and environmental operating conditions. This structured formulation facilitates the interpretation of the governing equations and their application within the numerical multiphysics framework.

The PEMFC model incorporates conservation equations for mass, momentum, chemical species, energy, electronic charge, and protonic charge. These equations are mutually coupled through the electrochemical reaction rates, heat generation, species consumption, water production, and membrane hydration.

2.2.1. Mass Conservation

The general continuity equation for the gas mixture is expressed as

$$\nabla \cdot (\varrho u) = S_m \quad (4)$$

where ϱ is the gas-mixture density, u is the velocity vector, and S_m represents the mass source or sink associated with electrochemical reactions and water generation.

For regions without volumetric mass generation, Equation (4) reduces to

$$\nabla \cdot (\varrho u) = 0 \quad (5)$$

2.2.2. Momentum Conservation

Momentum conservation within the gas-flow channels is described by

$$\nabla \cdot (\varrho u_u) = -\nabla p + \nabla \cdot [\mu(\nabla u + \nabla u^T)] + S_u \quad (6)$$

where p is pressure, μ is the dynamic viscosity, and S_u represents the momentum source term.

Within the porous gas diffusion and catalyst layers, the additional momentum resistance is represented using Darcy's law:

$$S_u = -(\mu/K)u \quad (7)$$

where K is the permeability of the porous medium.

The Darcy resistance accounts for the reduction in gas velocity resulting from the tortuous pathways through the porous electrodes.

2.2.3. Species Transport

The conservation equation for an individual gaseous species is written as

$$\nabla \cdot (\varrho u Y_i) = \nabla \cdot (\varrho D_{i,eff} \nabla Y_i) + S_i \quad (8)$$

where Y_i represents the mass fraction of species i, $D_{i,eff}$ is its effective diffusion coefficient, and S_i is the species source or sink resulting from electrochemical reactions or phase transfer.

The effective diffusivity within a porous medium is evaluated using the Bruggeman correction:

$$D_{i,eff} = \varepsilon^{1.5} D_i \quad (9)$$

where ε represents porosity and D_i is the corresponding bulk diffusion coefficient.

The molar consumption rate of hydrogen at the anode is related to local current density by Faraday's law:

$$N_{H_2} = j/(2F) \quad (10)$$

The corresponding oxygen consumption rate at the cathode is

$$N_{O_2} = j/(4F) \quad (11)$$

The electrochemical water-production rate is

$$N_{H_2O} = j/(2F) \quad (12)$$

where j represents local current density and F is Faraday's constant, equal to 96,485 C mol^{-1}.

These relationships directly couple electrochemical activity with hydrogen consumption, oxygen depletion, and water production.

2.2.4. Electronic and Protonic Charge Transport

Electronic charge conservation through the electrically conducting solid components is expressed as

$$\nabla\cdot(\sigma_s\nabla\varphi_s) + S_j = 0 \quad (13)$$

Protonic charge conservation within the membrane and ionomer-containing catalyst layers is described by

$$\nabla\cdot(\sigma_m\nabla\varphi_m) - S_j = 0 \quad (14)$$

where σ_s represents electronic conductivity, σ_m is protonic conductivity, φ_s is the solid-phase potential, φ_m is the membrane-phase potential, and S_j is the electrochemical current source.

The local activation overpotential is determined from

$$\eta = \varphi_s - \varphi_m - E_{eq} \quad (15)$$

where E_{eq} represents the equilibrium potential.

The local electrochemical reaction rate is calculated using the Butler–Volmer relationship:

$$j = j_0\,[\exp(\alpha_a F\eta/RT) - \exp(-\alpha_c F\eta/RT)] \quad (16)$$

where j_0 is the exchange current density, α_a and α_c are the anodic and cathodic charge-transfer coefficients, R is the universal gas constant, and T is the local absolute temperature.

To account for the dependence of the cathodic oxygen reduction reaction on oxygen availability, the relationship may be written as

$$j = j_0\,(CO_2/CO_{2,ref})^{\gamma}\,[\exp(\alpha_a F\eta/RT) - \exp(-\alpha_c F\eta/RT)] \quad (17)$$

where CO_2 represents the local oxygen concentration, $CO_{2,ref}$ is the reference oxygen concentration, and γ is the oxygen concentration exponent.

The reversible cell potential is calculated using the Nernst equation:

$$Erev = E^0(T) + (RT/2F)\,\ln[(pH_2 \times pO_2^{0.5})/pH_2O] \quad (18)$$

where $E^0(T)$ is the temperature-dependent standard equilibrium potential, while pH_2, pO_2, and pH_2O represent the partial pressures of hydrogen, oxygen, and water vapor, respectively.

This formulation allows environmental temperature and humidity to influence both electrochemical equilibrium and reaction kinetics.

2.2.5. Electrochemically Active Surface Area and Catalyst Durability Considerations

The electrochemically active surface area (ECSA) of platinum-based electrodes represents an important parameter governing catalyst utilization, oxygen reduction reaction kinetics, and the long-term electrochemical stability of proton exchange membrane fuel cells. ECSA describes the accessible platinum surface area available for electrochemical reactions and is commonly expressed relative to the platinum mass ($m^2\,gPt^{-1}$). Its magnitude depends on platinum particle size, catalyst dispersion, ionomer coverage, electrode microstructure, and the accessibility of electrochemical reaction sites. Temperature and relative humidity can influence effective catalyst utilization through changes in ionomer hydration, oxygen transport, and local electrochemical conditions. During prolonged operation, these environmental stresses may also contribute to irreversible ECSA deterioration through platinum dissolution, particle growth, agglomeration, and redistribution, depending on the electrochemical operating conditions.

The relationship between ECSA and the electrochemical reaction rate can be introduced through the exchange current density, which is influenced by the available platinum surface area. For a consistent reference basis, the apparent exchange current density may be expressed as

$$j_0 = i_{0,Pt} \times ECSA \times LP_t \quad (19)$$

where $i_{0,Pt}$ represents the platinum-specific exchange current density ($A.mPt^{-2}$), ECSA is the electrochemically active platinum surface area per unit platinum mass ($mPt^2\ kgPt^{-1}$), and LP_t is the platinum loading per unit electrode area ($kgP_t\ m^{-2}$). The resulting j_0 is expressed in A m^{-2} of electrode area. This relationship illustrates how variations in accessible platinum surface area may influence the activation losses and polarization characteristics of the fuel cell. The temperature dependence of the intrinsic platinum reaction kinetics and changes in oxygen availability must also be considered when interpreting the resulting electrochemical response.

In the present study, the electrochemical reaction kinetics are represented using the Butler–Volmer formulation, while the catalyst-layer properties remain fixed across the investigated temperature–humidity scenarios. Consequently, the numerical results characterize the effects of environmental conditions on electrochemical performance, membrane hydration, and reactant transport without explicitly resolving changes in platinum ECSA or irreversible catalyst degradation. A quantitative ECSA evaluation would require experimentally determined catalyst surface areas, such as those obtained through cyclic voltammetry or CO-stripping measurements, or an independently validated catalyst degradation model. Furthermore, predicting MEA lifespan would require transient simulations incorporating time-dependent platinum dissolution, particle growth, carbon-support degradation, and associated ECSA loss. These aspects are recognized as important extensions of the present environmental resilience framework, particularly for distinguishing reversible performance deterioration from irreversible catalyst aging under prolonged temperature–humidity exposure.

2.3. Membrane Hydration and Water Transport Model

Membrane hydration is one of the principal physical mechanisms considered in this study because proton conductivity in PEMFC membranes strongly depends on water content. Insufficient hydration increases membrane resistance, whereas excessive water can contribute to cathode flooding and oxygen-transport limitations.

The membrane water content, λ, is defined as the number of water molecules associated with each sulfonic-acid group:

$$\lambda = nH_2O/nSO_3^- \quad (20)$$

The local water activity is defined as

$$a = pH_2O/P_{sat}(T) \quad (21)$$

where pH_2O is the local water-vapor partial pressure and $P_{sat}(T)$ represents the saturation vapor pressure of water at the local temperature.

For a vapor-equilibrated Nafion-type membrane, the equilibrium membrane water content can be described by

$$\lambda = 0.043 + 17.81a - 39.85a^2 + 36.0a^3;\ 0 \le a \le 1 \quad (22)$$

For water activity above unity, the relationship becomes

$$\lambda = 14 + 1.4(a - 1);\ 1 < a \le 3 \quad (23)$$

Water transport across the membrane is primarily controlled by electro-osmotic drag and back diffusion. Electro-osmotic drag transports water from the anode toward the

cathode together with proton movement, whereas back diffusion generally transports water from the wetter cathode region toward the anode.

The net water flux through the membrane is represented as

$$N_w = n_d(j/F) - D_w C_f \nabla\lambda \quad (24)$$

where N_w is the net membrane water flux, n_d is the electro-osmotic drag coefficient, D_w is the water diffusion coefficient within the membrane, and C_f is the concentration of fixed ionic sites.

Under steady-state conditions, water conservation within the membrane becomes

$$\nabla \cdot N_w = 0 \quad (25)$$

The proton conductivity of the membrane is described as a function of membrane water content and temperature:

$$\sigma_m = (0.5139\lambda - 0.326) \exp[1268(1/303 - 1/T)] \quad (26)$$

Equation (25) provides a direct coupling between environmental conditions and electrochemical performance. A decrease in relative humidity reduces membrane water content, which lowers proton conductivity and increases ohmic losses. Conversely, increasing humidity generally improves membrane hydration but can eventually increase liquid-water accumulation and mass-transfer resistance.

Water management within the PEMFC involves coupled vapor transport, electrochemical water production, membrane hydration, and liquid-water formation. Local condensation and evaporation are governed by the relationship between the water-vapor partial pressure and the temperature-dependent saturation pressure. Accordingly, the local vapor activity is evaluated as the ratio between these pressures, consistent with Equation (20). When the local vapor partial pressure exceeds the saturation pressure, the gas phase becomes supersaturated, providing a thermodynamic driving force for condensation. Conversely, evaporation may occur when liquid water is present and the surrounding gas remains undersaturated. These processes influence the distribution of water between the gas and liquid phases and consequently affect oxygen accessibility, membrane hydration, and electrochemical performance.

A possible representation of the net condensation–evaporation rate is based on the local difference between water-vapor concentration and saturation concentration. The resulting phase-change source term can be incorporated into the water-vapor species conservation equation, with an equal and opposite contribution to liquid-water conservation. The saturation concentration is evaluated using the local temperature, allowing non-uniform thermal conditions to influence condensation and evaporation. Within porous electrodes, liquid-water accumulation may additionally reduce the effective gas-filled porosity and oxygen diffusivity, thereby increasing mass-transport resistance. A physically consistent implementation requires the specification of phase-change kinetic coefficients, liquid-water transport properties, and the coupling between saturation and effective gas-phase transport.

The inlet vapor concentration is prescribed through the temperature-dependent relative humidity, as defined by Equations (41) and (42), whereas local vapor conditions must be determined from the coupled species and energy conservation equations. This distinction is particularly important because the local relative humidity can differ from the inlet value due to electrochemical water production, temperature gradients, and water transport. Explicitly resolving these interactions would provide a more complete mechanistic description of the transition between dehydration-prone and flooding-prone operating conditions.

Water management in the PEMFC is governed by the coupled effects of electrochemical water generation, membrane hydration, electro-osmotic drag, back diffusion, evaporation, condensation, and liquid-water accumulation within the porous electrodes. Water produced by the oxygen reduction reaction at the cathode catalyst layer may remain in the vapor phase or condense when the local water-vapor partial pressure exceeds the saturation pressure corresponding to the local temperature. Conversely, evaporation is favored when the local vapor pressure falls below saturation. The resulting liquid-water accumulation is characterized by the local saturation, defined as the fraction of available pore volume occupied by liquid water. Increasing liquid-water saturation reduces the pore space available for reactant transport and may consequently restrict oxygen accessibility to the catalyst layer, particularly under highly humidified operating conditions. The coupled electrochemical, thermal, and transport responses are governed by the exchange current density, charge-transfer coefficients, electronic and protonic conductivities, membrane water diffusivity, electro-osmotic drag coefficient, porous-medium permeability, effective species diffusivity, and thermal conductivity. The temperature- and hydration-dependent relationships introduced in the governing equations are used to describe the corresponding variations in transport and electrochemical behavior. These mechanisms are consistent with established PEMFC water-management and multiphase-transport frameworks, in which the balance between membrane hydration, vapor transport, and liquid-water removal determines the transition between dehydration-dominated and flooding-prone operating conditions.

2.4. Thermal Transport and Heat Generation

The temperature distribution throughout the PEMFC is obtained from the energy conservation equation:

$$\nabla\cdot(\varrho C_p\, uT) = \nabla\cdot(k_{eff}\nabla T) + ST \tag{27}$$

where C_p is the specific heat capacity, k_{eff} is the effective thermal conductivity, and ST represents the volumetric heat-source term.

The total heat generated within the PEMFC consists primarily of activation, ohmic, and reversible entropic contributions:

$$Q_{gen} = Q_{act} + Q_{ohm} + Q_{rev} \tag{28}$$

Ohmic heat generation is expressed as

$$Q_{ohm} = j^2/\sigma \tag{29}$$

The reversible entropic heat contribution is expressed as

$$Q_{rev} = -jT(\partial E_{rev}/\partial T) \tag{30}$$

Temperature strongly interacts with water transport. Increasing temperature increases the saturation vapor pressure of water and facilitates evaporation, which can reduce liquid-water accumulation. However, at low relative humidity, elevated temperature can intensify membrane dehydration. Conversely, decreasing temperature promotes condensation and can increase liquid-water saturation within porous cathode regions. Consequently, temperature and relative humidity must be evaluated simultaneously when assessing environmental resilience.

2.5. Environmental Temperature and Relative-Humidity Stress Scenarios

A systematic temperature–humidity matrix was established to investigate PEMFC behavior across different environmental stress conditions. Four temperature levels and four relative-humidity levels were selected, producing 16 environmental scenarios. This factorial approach enables the individual and combined effects of temperature and humidity to be distinguished and provides sufficient data for constructing environmental response maps.

The 16 temperature–humidity scenarios presented in Table 2 represent controlled reactant-inlet operating conditions rather than direct measurements or predictions of ambient climatic conditions. The prescribed temperature corresponds to the reactant inlet temperature, while the relative humidity defines the water-vapor content of the supplied reactant streams. These quantities should be distinguished from the ambient temperature surrounding the fuel-cell assembly and from the local operating temperature within the membrane–electrode assembly, which is governed by the coupled energy conservation equation and internal heat-generation mechanisms. Accordingly, the terms cold, warm, hot, dry, and humid are used as descriptive classifications of the imposed inlet conditions rather than as direct representations of geographical climates. The investigated scenarios are intended to characterize the sensitivity of PEMFC performance to controlled thermal and humidification stresses, providing a basis for evaluating operating limitations relevant to variable environmental exposure without assuming a direct equivalence between ambient and internal operating conditions.

Table 2. Temperature and relative-humidity environmental stress scenarios.

Case	Temperature (°C)	Relative Humidity (%)	Environmental Condition
C1	20	20	Cold–dry
C2	20	50	Cold–moderate
C3	20	80	Cold–humid
C4	20	100	Cold–saturated
C5	40	20	Mild–dry
C6	40	50	Mild–moderate
C7	40	80	Mild–humid
C8	40	100	Mild–saturated
C9	60	20	Warm-dry
C10	60	50	Warm–moderate
C11	60	80	Warm–humid/reference
C12	60	100	Warm–saturated
C13	80	20	Hot–dry
C14	80	50	Hot–moderate
C15	80	80	Hot–humid
C16	80	100	Hot–saturated

The condition of 60 °C and 80% relative humidity, represented by C11, is adopted as the reference condition for normalized comparisons. The remaining geometrical, material, flow, pressure, and electrical parameters are maintained constant across the environmental scenarios.

This environmental matrix is designed as a controlled stress-testing framework rather than as a direct prediction of specific future climatic conditions. It allows the transition from dehydration-dominated to balanced and flooding-dominated operation to be systematically investigated.

The temperature–humidity combinations investigated in this study are intended to provide a systematic environmental stress-testing framework rather than reproduce the complete range of operating conditions encountered in specific automotive or stationary PEMFC systems. In practical applications, stack operating temperature and reactant relative humidity are influenced by thermal management, humidification strategies, cooling-system performance, reactant recirculation, and electrical load, and therefore do not necessarily correspond directly to ambient environmental conditions. Automotive PEMFC systems commonly operate under actively controlled thermal and water-management conditions, whereas stationary applications may employ different operating temperatures and humidification strategies depending on their system configuration and duty cycle. Consequently, the investigated temperature range of 20–80 °C and relative-humidity range of 20–100% should be interpreted as a controlled parametric envelope designed to examine the sensitivity of electrochemical performance and transport phenomena to coupled thermal and moisture stresses. The lower-temperature conditions provide insight into cold-operation and thermal-management limitations, while elevated-temperature and low-humidity combinations represent dehydration-prone operating states. Conversely, highly humidified conditions enable the investigation of condensation-related water accumulation and oxygen-transport restrictions. Although not all investigated combinations represent typical continuous operating conditions in commercial PEMFC systems, their systematic evaluation facilitates the identification of physical response mechanisms, limiting operating regimes, and temperature–humidity interactions that may become relevant during off-design operation or insufficient thermal and water management. Accordingly, the findings should be interpreted as a mechanistic assessment of environmental sensitivity and resilience rather than a direct prediction of application-specific automotive or stationary performance. Further validation under representative system operating profiles, including transient loads, realistic inlet conditions, and application-specific thermal-management constraints, would be required to extend the framework toward direct operational predictions.

2.6. Environmental Resilience Indicators and Performance Metrics

In the context of the present investigation, environmental resilience is defined as the relative ability of a PEMFC to preserve its electrochemical performance and essential internal transport functions when subjected to prescribed temperature–humidity stresses. This definition refers specifically to steady-state performance retention and environmental tolerance rather than dynamic recovery, autonomous adaptation, or long-term resistance to irreversible degradation. Accordingly, resilience is evaluated through the combined consideration of voltage and power-density retention, membrane hydration, oxygen availability, spatial current-density uniformity, and the associated transport limitations. The Environmental Resilience Index (ERI), together with the individual performance indicators, provides a comparative framework for identifying operating conditions under which the cell maintains favourable electrochemical and transport characteristics relative to the reference condition. Therefore, the term resilience is employed in a restricted, operationally defined sense and should not be interpreted as evidence of transient recovery behaviour or experimentally demonstrated durability.

Environmental resilience cannot be adequately characterized by cell voltage alone. Accordingly, several performance, transport, hydration, and uniformity indicators are employed to quantify the ability of the PEMFC to maintain stable operation under temperature and humidity extremes.

Voltage retention relative to the reference environmental condition is defined as

$$R_V = V_{(T,RH)}/V_{ref} \quad (31)$$

where $V_{(T,RH)}$ is the cell voltage under a specific environmental condition and V_{ref} is the corresponding voltage under the reference condition at the same electrical load.

Power-density retention is similarly calculated as

$$R_P = P_{(T,RH)}/P_{ref} \quad (32)$$

where P is the calculated power density and Pref represents the reference power density.

The power density is calculated from

$$P = V \times j \quad (33)$$

Membrane hydration retention is evaluated using

$$R\lambda = \lambda_{avg}(T,RH)/\lambda_{avg,ref} \quad (34)$$

where λ_{avg} represents the spatially averaged membrane water content.

Spatial current-density uniformity is evaluated through the coefficient of variation:

$$CV_j = \sigma_j/j_{avg} \quad (35)$$

where σ_j is the standard deviation of local current density and j_{avg} is its spatial average.

A lower value of CV_j represents a more uniform electrochemical reaction distribution, whereas increasing CV_j indicates stronger localized electrochemical activity and potentially greater susceptibility to local degradation.

Thermal nonuniformity is evaluated using

$$\Delta T = T_{max} - T_{min} \quad (36)$$

where T_{max} and T_{min} represent the maximum and minimum temperatures within the computational domain.

Oxygen-transport resilience is evaluated using the normalized minimum oxygen concentration:

$$RO_2 = CO_{2,min}/CO_{2,in} \quad (37)$$

where $CO_{2,min}$ is the minimum local oxygen concentration and $CO_{2,in}$ is the cathode inlet oxygen concentration.

Liquid-water accumulation within the porous cathode region is evaluated from the volume-averaged liquid-water saturation:

$$S_{l,avg} = (1/V_p) \int S_l \, dV \quad (38)$$

where S_l represents local liquid-water saturation and V_p represents the volume of the investigated porous region.

Based on these parameters, three principal environmental response regimes are considered. (See Table 3).

Table 3. Classification of the principal PEMFC environmental response regimes.

Regime	Environmental Tendency	Dominant Mechanism	Expected PEMFC Response
Regime I	High temperature and low RH	Membrane dehydration	Reduced proton conductivity and increased ohmic losses
Regime II	Balanced temperature and RH	Balanced hydration and water removal	Stable electrochemical and transport performance
Regime III	High humidity/condensation-prone conditions	Liquid-water accumulation	Oxygen transport limitation and concentration losses

The actual boundaries among these regimes are not predetermined. Instead, they are identified from the calculated membrane hydration, liquid-water saturation, oxygen availability, current-density distribution, and electrochemical performance.

To provide an integrated measure of environmental performance, an Environmental Resilience Index (ERI) can be formulated as

$$ERI = w1RV + w2RP + w3R\lambda + w4(1 - CV_{j,norm}) + w5RO_2 \quad (39)$$

where w1 to w5 represent weighting factors assigned to the individual resilience indicators.

The weighting factors satisfy

$$w1 + w2 + w3 + w4 + w5 = 1 \quad (40)$$

Equal weighting ($w_1 = w_2 = w_3 = w_4 = w_5 = 0.20$) is adopted as a neutral baseline to avoid assigning subjective priority to any individual resilience mechanism. The indicators are evaluated at a common current density, using C11 (60 °C, 80% RH) as the reference condition. Voltage, power density, and membrane hydration are normalized using their corresponding reference values, whereas oxygen-transport resilience is evaluated using Equation (40). Current-density non-uniformity is expressed through its normalized coefficient of variation, with lower values indicating greater uniformity. The resulting ERI provides a comparative measure of environmental performance rather than an absolute measure of PEMFC durability.

For an equal-weight baseline assessment:

$$w1 = w2 = w3 = w4 = w5 = 0.20 \quad (41)$$

The composite ERI is intended to complement rather than replace the individual physical indicators. Accordingly, voltage, power density, hydration, oxygen availability, and current-density uniformity are also analyzed independently in the Section 3.

The maximum admissible current density is defined as the highest operating current density at which the prescribed electrochemical and transport constraints are simultaneously satisfied. These constraints include maintaining the cell voltage above its minimum allowable value, membrane water content above the dehydration threshold, local oxygen concentration above the oxygen-starvation limit, and liquid-water saturation below the flooding threshold. The admissible operating limit is determined by evaluating these criteria across the simulated polarization range, with the first violated constraint defining the maximum sustainable current density. This approach provides a consistent framework for identifying the operating limits under different temperature–humidity conditions.

2.7. Boundary Conditions and Numerical Implementation

Hydrogen is supplied to the anode inlet, while humidified air is supplied to the cathode inlet. For each environmental scenario, the inlet temperature and water-vapor concentration are adjusted according to the prescribed temperature and relative humidity.

The water-vapor partial pressure is calculated as

$$pH_2O = RH \times P_{sat}(T) \quad (42)$$

where RH is expressed as a fraction between 0 and 1.

The corresponding inlet water-vapor mole fraction is determined from

$$xH_2O = pH_2O/P_{in} \quad (43)$$

where P_{in} represents the total inlet pressure.

The inlet temperature and relative humidity are prescribed independently of the local thermal and hydration fields calculated within the computational domain. The inlet water-vapor partial pressure is determined using the saturation vapor pressure at the corresponding inlet temperature, as described by Equation (41), while Equation (42) provides the associated water-vapor mole fraction. For a complete description of reactant

humidification, the anode and cathode inlet conditions are distinguished through the quantities $RH_{a,in}$ and $RH_{c,in}$, respectively, with their corresponding vapor partial pressures expressed as $pH_2O,_{a,in} = RH_{a,in} \times P_{sat}(T_{a,in})$ and $pH_2O,_{c,in} = RH_{c,in} \times P_{sat}(T_{c,in})$. These expressions allow the two reactant streams to be specified independently and distinguish inlet humidification from local water activity within the membrane–electrode assembly.

The thermal behavior of the PEMFC is governed by the non-isothermal energy conservation equation presented in Section 2.4, which incorporates heat conduction, convective energy transport, and volumetric heat generation associated with activation, ohmic, and reversible entropic contributions. The resulting internal temperature distribution is therefore not necessarily equal to the prescribed reactant inlet temperature. Thermal interactions involving the external walls, bipolar plates, coolant, and surrounding environment require appropriate boundary specifications, including imposed temperature, heat flux, or convective heat transfer conditions, depending on the physical configuration represented. In the absence of an explicitly resolved coolant domain or external heat-exchange model, the results should be interpreted as a cell-level assessment of imposed inlet thermal conditions rather than as predictions of the complete stack thermal-management response. This distinction is particularly important when extrapolating the present findings to practical automotive, stationary, or maritime PEMFC installations.

Representative baseline operating conditions are summarized in Table 4.

The prescribed inlet relative humidity determines the initial water-vapor content of the reactant streams, whereas the local vapor distribution depends on species transport, electrochemical water generation, and temperature-dependent saturation conditions. Consequently, the inlet humidity should not be interpreted as a uniform relative-humidity value throughout the computational domain. Local vapor conditions must be evaluated consistently with the species and thermal transport equations when assessing membrane hydration and the potential for condensation or evaporation.

The computational framework considers a three-dimensional, steady-state, non-isothermal PEMFC configuration in which mass, momentum, species, electronic charge, protonic charge, membrane water transport, and energy conservation equations are coupled through electrochemical reaction and transport source terms. The numerical solution is obtained iteratively, accounting for the dependence of local electrochemical kinetics on oxygen concentration, temperature, and activation overpotential, while membrane proton conductivity depends on temperature and water content. The porous GDL and CL regions are represented as homogeneous media with Darcy-type momentum resistance, and their effective transport properties are incorporated into the governing equations.

For numerical reproducibility, the computational implementation is characterized by the discretization of the governing conservation equations, treatment of pressure–velocity coupling, nonlinear source-term linearization, convergence monitoring, and mesh-refinement assessment. In a pressure-based finite-volume implementation, a consistent reference strategy comprises second-order spatial discretization for momentum, species, and energy transport, SIMPLE pressure–velocity coupling, and iterative treatment of the electrochemical and membrane-water source terms. Residual tolerances of 10^{-5} for continuity, momentum, species, and charge conservation and 10^{-6} for energy, together with under-relaxation factors of 0.3 for pressure, 0.7 for momentum, and 0.9 for energy, constitute a possible reference configuration. These numerical settings are presented as a reproducible implementation specification rather than independently verified settings of the original simulations.

The principal electrochemical, porous-medium, thermal, and membrane-transport parameters are consolidated in Table 5. Literature-based reference parameters are selected

from established PEMFC modeling studies, including the three-dimensional modeling work of Meng and the membrane water-transport formulation of Springer et al. The adopted reference set distinguishes volumetric exchange current densities from surface-based kinetic parameters and preserves the temperature- and hydration-dependent character of membrane transport. Geometrical parameters and operating conditions remain consistent with the values reported in Tables 1 and 4.

Numerical convergence is assessed by monitoring the residual behavior of the governing equations and the stabilization of cell voltage, total current, average membrane water content, outlet species concentrations, and maximum temperature. Mesh independence is evaluated using approximately 200,000, 400,000, 800,000, and 1,200,000 computational elements. The corresponding cell voltages of 0.681, 0.695, 0.701, and 0.703 V indicate progressively reduced mesh sensitivity. The relative voltage difference between the two finest grids is approximately 0.29%, supporting the adequacy of the refined spatial discretization for the reported voltage prediction. The numerical framework maintains identical geometrical and operating definitions, apart from the prescribed temperature and relative humidity, across the 16 environmental scenarios.

Table 4. Baseline operating conditions for the environmental-stress simulations.

Parameter	Baseline Condition
Anode reactant	Hydrogen
Cathode reactant	Air
Operating pressure	1 atm
Hydrogen stoichiometric ratio	1.5
Air stoichiometric ratio	2.0
Reference temperature	60 °C
Reference relative humidity	80%
Investigated temperature range	20–80 °C
Investigated RH range	20%, 50%, 80%, 100%
Simulation condition	Steady state
Flow regime	Laminar
Gas behavior	Ideal mixture
Anode volumetric exchange current density	1.0×10^{9}
Cathode volumetric exchange current density	1.0×10^{4}
Anodic charge-transfer coefficient	1.0
Cathodic charge-transfer coefficient	1.0
GDL permeability	1.0×10^{-12}
CL permeability	1.0×10^{-13}
GDL porosity	0.7
CL porosity	0.4
Effective electronic conductivity of CL/GDL	5.0×10^{3}
Electro-osmotic drag coefficient at (λ =14)	1.59
Electro-osmotic drag coefficient at ($\lambda = 22$)	2.5
GDL thickness	3.0×10^{-4}
CL thickness	1.0×10^{-5}
Membrane thickness	5.0×10^{-5}
Hydrogen stoichiometric ratio	1.5
Air stoichiometric ratio	2.0

Table 5. Framework for the mesh-independence assessment.

Mesh	Approximate Number of Elements	Cell Voltage (V)	Difference from Previous Mesh (%)
M1—Coarse	200,000	0.681	–
M2—Medium	400,000	0.695	2.06
M3—Fine	800,000	0.701	0.86
M4—Very fine	1,200,000	0.703	0.29

To clarify the inlet flow-rate specification, the hydrogen and air stoichiometric ratios of 1.5 and 2.0, respectively, are treated as prescribed operating targets. Under a constant-stoichiometry approach, the reactant inlet flow rates are adjusted at each polarization-curve operating point according to the corresponding current density. The required molar flow rates are calculated as $\dot{n}_{H_2,in} = 1.5IA/(2FA)$ and $\dot{n}_{air,in} = 2.0IA/(4Fx_{O_2}A)$, where I is the total cell current, F is Faraday's constant, A is the active area, and x_{O_2} is the oxygen mole fraction in the humidified inlet air. Equivalently, using current density j, $\dot{n}_{H_2,in} = 1.5jA/(2F)$ and $\dot{n}_{air,in} = 2.0jA/(4Fx_{O_2}F)$. Thus, the inlet flow rates remain constant only within an individual steady-state operating point, rather than throughout the complete polarization sweep. Oxygen utilization is evaluated from the ratio of oxygen consumption to oxygen supply, while the pressure drop and air-pumping power are evaluated using the flow conditions corresponding to each operating point. This treatment maintains consistency between reactant consumption, inlet flow rates, and electrochemical loading.

A no-slip boundary condition is imposed at the solid walls of the flow channels. At the outlets, pressure boundary conditions are applied. Appropriate electrical boundary conditions are imposed at the current collectors, while continuity of temperature, heat flux, species transport, and electrical or ionic potential is maintained across the relevant internal interfaces.

The governing equations are solved simultaneously using an iterative numerical procedure. Convergence is assessed using both residual criteria and the stability of important integral parameters. Cell voltage, total current, average membrane water content, outlet species concentrations, and maximum temperature are monitored during the iterative solution. A simulation is considered converged only when the residual requirements are satisfied and these physical parameters remain stable with further iterations.

To establish a consistent and reproducible framework for evaluating the system-level performance of the proton exchange membrane fuel cell (PEMFC), the air-supply requirements, pumping power, net electrical power density, hydrogen consumption rate, and energy-conversion efficiency were determined using electrochemical and thermodynamic relationships. The same calculation procedure was applied to all 16 temperature–relative-humidity scenarios, while the prescribed hydrogen and air stoichiometric ratios were maintained at 1.5 and 2.0, respectively.

The hydrogen and air molar supply rates were calculated from Faraday's law:

(1) Hydrogen molar supply rate

$$\dot{n}_{H_2,in} = (\lambda_{H_2} \times I)/(2 \times F) \quad (44)$$

(2) Air molar supply rate

$$\dot{n}_{air,in} = (\lambda_{air} \times I)/(4 \times F \times x_{O_2}) \quad (45)$$

where I is the total cell current (A), F is Faraday's constant (96,485 C/mol), $\lambda_{H_2} = 1.5$ is the hydrogen stoichiometric ratio, $\lambda_{air} = 2.0$ is the air stoichiometric ratio, and $x_{O_2} = 0.21$ represents the oxygen mole fraction in dry air. The volumetric air-flow rate was subsequently estimated using the ideal-gas equation:

(3) Air volumetric flow rate

$$V_{air} = (\dot{n}_{air,in} \times R \times T_{in})/P_{in} \quad (46)$$

where V_{air} is the volumetric air-flow rate (m^3/s), R is the universal gas constant (8.314 J/mol·K), T_{in} is the absolute inlet temperature (K), and P_{in} is the absolute inlet pressure (Pa). For humidified air, the volumetric flow rate should be calculated using the total wet-gas molar flow rate, including water vapor.

The electrical power required to supply air was estimated using the pressure rise across the air-supply system and the blower efficiency:

(4) Air-pumping power

$$P_{pump} = (\Delta P \times V_{air})/\eta_b \quad (47)$$

where P_{pump} is the air-pumping power (W), ΔP is the pressure rise across the air-supply system (Pa), and η_b is the overall blower efficiency. This relationship assumes a low-pressure-rise blower with approximately incompressible gas-flow behavior. For a compressor operating at a substantial pressure ratio, a compressible-gas power model is required instead.

The gross electrical power and gross power density were calculated as:

(5) Gross electrical power

$$P_{gross} = V_{cell} \times I \quad (48)$$

(6) Gross electrical power density

$$p_{gross} = V_{cell} \times j \quad (49)$$

where V_{cell} is the operating cell voltage (V) and j is the current density (A/cm^2). The net electrical power was determined by subtracting the air-pumping requirement from the gross electrical output:

(7) Net electrical power

$$P_{net} = P_{gross} - P_{pump} \quad (50)$$

(8) Net electrical power density

$$P_{net} = P_{gross} - (P_{pump}/A_{act})$$

where A_{act} is the active cell area (cm^2). Accordingly, the net power density represents the useful electrical output after accounting for the air-supply power requirement. If additional auxiliary components are included in the system boundary, their electrical consumption must also be subtracted.

The electrochemically consumed hydrogen mass-flow rate was calculated from Faraday's law:

(9) Hydrogen consumption rate

$$m_{H2,cons} = (I \times M_{H2})/(2 \times F) \quad (51)$$

where M_{H2} = 0.002016 kg/mol is the molar mass of hydrogen. This expression represents the hydrogen consumed by the electrochemical reaction, whereas the supplied hydrogen flow rate is greater because of the prescribed hydrogen stoichiometric ratio.

The net electrical efficiency was defined as the ratio of useful net electrical power to the chemical energy released by the consumed hydrogen:

(10) Net electrical efficiency based on LHV

$$\eta_{net,LHV} = [P_{net}/(m_{H2,cons} \times LHV_{H2})] \times 100\% \quad (52)$$

where LHV_{H2} is the lower heating value of hydrogen, approximately 120 MJ/kg. If the higher heating value (HHV) is adopted, the corresponding value is approximately 142 MJ/kg and must be used consistently throughout the analysis.

For comparisons across different temperature–humidity scenarios, all system-level indicators were evaluated using the same prescribed operating-load selection criterion. The selected current density, the air-supply pressure rise, and the blower efficiency were applied consistently to the calculations, allowing the influence of temperature and humidity to be assessed without introducing differences arising from inconsistent system-level assumptions.

The system-level performance of the PEMFC was evaluated using a consistent thermodynamic and electrochemical framework to quantify air-pumping power, net electrical power density, hydrogen consumption, and energy-conversion efficiency under the 16 investigated temperature–relative-humidity operating scenarios. The hydrogen and air stoichiometric ratios were maintained at 1.5 and 2.0, respectively, and the corresponding reactant molar supply rates were determined from Faraday's law as $n_{H2,in} = \lambda_{H2}I/(2F)$ and $n_{air,in} = \lambda_{air}I/(4Fx_{O2})$, where I represents the operating current, F is Faraday's constant (96,485 C/mol), and $x_{O2} = 0.21$ is the oxygen mole fraction in dry air. The volumetric air-flow rate was calculated using the ideal-gas relationship, $V_{air} = \dot{n}_{air,in}RT_{in}/P_{in}$, where R = 8.314 J/(mol·K), T_{in} is the absolute inlet temperature, and P_{in} is the absolute inlet pressure. For humidified inlet air, the total volumetric flow rate includes the water-vapor contribution. The electrical power required for air delivery was estimated using $P_{pump} = \Delta P\ V_{air}/\eta_b$, where ΔP denotes the required air-supply pressure rise and η_b represents the overall blower efficiency. This expression assumes low-pressure-ratio operation with approximately incompressible gas-flow behavior. Gross electrical power was calculated as $P_{gross} = V_{cell\ I}$, whereas net electrical power was determined by subtracting the air-pumping requirement, $P_{net} = P_{gross} - P_{pump}$. Accordingly, net electrical power density was defined as $P_{net} = V_{cell\ j} - P_{pump}/A_{act}$, where j is the operating current density and A_{act} is the electrochemically active area. The hydrogen consumption rate was determined from $m_{H2,cons} = IM_{H2}/(2F)$, where $M_{H2} = 0.002016$ kg/mol represents the molar mass of hydrogen. The net electrical energy-conversion efficiency was evaluated using $\eta_{net,LHV} = [P_{net}/(m_{H2,cons} \times LHV_{H2})] \times 100\%$, adopting the lower heating value of hydrogen ($LHV_{H2} \approx 120$ MJ/kg). The same calculation methodology was applied consistently to all operating scenarios, with the system-level indicators evaluated according to a common operating-load selection criterion to distinguish the effects of temperature and relative humidity from differences in electrical loading. This unified approach establishes a transparent relationship between the simulated electrochemical response and the resulting system-level performance indicators.

The environmental implications of PEMFC operation were considered separately from direct electrochemical emissions, which are zero for CO_2 during hydrogen oxidation. A complete lifecycle carbon assessment would require accounting for hydrogen production, compression, storage, transportation, electricity consumption by auxiliary equipment, and relevant manufacturing and end-of-life processes. For an operational fuel-supply assessment, the specific carbon intensity can be expressed as $CI = [(m_{H2} \times EF_{H2}) + (P_{aux} \times EF_{el})]/P_{net}$, where m_{H2} is the hydrogen supply rate (kg/h), EF_{H2} is the upstream hydrogen carbon-emission factor (kg CO_2e/kg H_2), P_{aux} is the externally supplied auxiliary electrical power (kW), EF_{el} is the carbon intensity of the auxiliary electricity (kg CO_2e/kWh), and P_{net} is the net delivered electrical power (kW). The resulting CI is expressed in kg CO_2e/kWh and can be converted to g CO_2e/kWh by multiplying by 1000. When auxiliary power is supplied internally by the fuel-cell system, its effect is incorporated through the reduction in net electrical output and must not be counted again as externally supplied electricity. The calculated carbon intensity depends on the hydrogen-production pathway, upstream electricity mix, system boundary, and auxiliary-energy assumptions. A sensitivity assessment can therefore be performed by varying EF_{H2} and EF_{el} across clearly specified low-, reference-, and high-carbon scenarios

while maintaining consistent operating conditions. Because the present electrochemical model does not independently establish these upstream emission factors or a complete lifecycle inventory, the numerical carbon-intensity estimates should not be interpreted as verified lifecycle emissions. Accordingly, the environmental discussion is limited to the dependence of potential upstream emissions per unit of delivered electricity on PEMFC operating performance, rather than claiming an independently validated lifecycle carbon footprint.

The numerical implementation was based on a three-dimensional, steady state, multiphysics formulation that simultaneously accounts for fluid flow, multicomponent species transport, heat transfer, electrochemical reactions, and electronic and protonic charge conservation. The governing equations were solved through an iterative numerical procedure incorporating the coupled interactions among the gas-flow channels, porous diffusion layers, catalyst layers, and polymer electrolyte membrane. Numerical convergence was evaluated by examining the residuals of the governing conservation equations and monitoring the stability of the predicted cell voltage, total current, average membrane water content, outlet species concentrations, and maximum temperature. Convergence was considered achieved when the governing-equation residuals satisfied the prescribed convergence requirements and the monitored physical variables remained stable during successive iterations. The same numerical solution and convergence-assessment procedure was applied consistently to all 16 temperature–relative-humidity scenarios to ensure comparability of the predicted electrochemical, thermal, and transport responses.

To characterize spatial non-uniformities, the local temperature, current density, oxygen concentration, membrane water content, and liquid-water saturation fields were considered within their corresponding computational regions. Spatial variations were evaluated using the local field values rather than relying exclusively on domain-averaged quantities. For membrane hydration, the normalized distributions represent the statistical distribution of local membrane water-content values over the membrane domain, with the distribution normalized to facilitate comparison between operating scenarios. Such distributions describe the frequency of different hydration states but do not preserve their spatial locations. Accordingly, local contour representations provide complementary information by identifying the positions of dehydration, oxygen depletion, temperature gradients, current-density localization, and liquid-water accumulation. For consistent comparison, the representative operating conditions C11 (60 °C, 80% RH) and C13 (80 °C, 20% RH) were selected to illustrate the differences between favorable and hot–dry operating environments.

The temperature and relative humidity values investigated in this study represent prescribed reactant inlet conditions rather than independently imposed ambient atmospheric conditions. Accordingly, hydrogen and humidified air enter the computational domain at the specified temperature and humidity levels, while the local cell temperature is determined through the coupled energy conservation equation, accounting for electrochemical heat generation and heat transfer within the cell components. Thermal continuity is maintained across the internal interfaces, allowing temperature gradients to develop within the computational domain. Therefore, the prescribed inlet temperature should not be interpreted as a spatially uniform operating temperature throughout the PEMFC.

2.8. Mesh Independence and Experimental Validation Limitations

A systematic mesh-independence assessment is performed to ensure that the predicted PEMFC response is independent of numerical grid resolution. Progressive refinement is particularly important across the membrane, catalyst layers, and gas

diffusion layers because these relatively thin regions contain steep gradients in species concentration, membrane hydration, electrical potential, current density, and temperature.

Four progressively refined computational grids are considered, as summarized in Table 5.

The percentage difference between two consecutive meshes is calculated as

$$\text{Difference (\%)} = |V_{new} - V_{previous}|/V_{previous} \times 100 \quad (53)$$

The final mesh is selected when additional refinement produces only a negligible variation in predicted cell voltage and other important physical quantities while substantially increasing computational cost. Mesh quality is additionally evaluated to ensure adequate resolution throughout the thin MEA components.

The numerical reliability of the present model was assessed through the mesh-independence analysis summarized in Table 5. Increasing the mesh resolution from approximately 800,000 to 1,200,000 elements changed the predicted cell voltage from 0.701 to 0.703 V, corresponding to a relative difference of approximately 0.29%. This result demonstrates limited grid sensitivity for the investigated operating point. However, mesh independence should be distinguished from experimental validation. Although Equations (44) and (45) define the mean absolute percentage error (MAPE) and root-mean-square error (RMSE), respectively, a matched experimental polarization dataset is not established in the present analysis. Consequently, quantitative MAPE and RMSE values cannot be reported, and agreement between simulated and experimental polarization curves, particularly in the high-current-density region, remains unverified. Differences in experimental cell geometry, membrane–electrode assembly properties, operating pressure, reactant humidification, and thermal boundary conditions may substantially influence polarization behavior and must be considered before transferring validation conclusions between different PEMFC configurations. Accordingly, the present results should be interpreted as a mesh-verified numerical assessment of temperature–humidity effects, while direct experimental validation remains necessary to establish quantitative predictive accuracy.

The mean absolute percentage error (MAPE) is calculated as

$$\text{MAPE} = (100/N)\ \Sigma\ |(V_{exp} - V_{sim})/V_{exp}| \quad (54)$$

where V_{exp} represents the experimentally measured voltage, V_{sim} represents the numerically predicted voltage, and N is the total number of experimental data points.

The root-mean-square error is additionally determined as

$$\text{RMSE} = \sqrt{[(1/N)\ \Sigma(V_{sim} - V_{exp})^2]} \quad (55)$$

The combination of graphical polarization comparison, MAPE, and RMSE provides both qualitative and quantitative measures of model accuracy. Attention is given to the high-current-density region because this operating range is strongly affected by oxygen depletion and water accumulation and is therefore important for evaluating the ability of the model to reproduce mass-transfer limitations.

The mesh-sensitivity results in Table 5 show that the predicted cell voltage approaches a grid-independent value with progressive refinement. Increasing the mesh resolution from 800,000 (M3) to 1,200,000 elements (M4) changes the cell voltage from 0.701 to 0.703 V, corresponding to a relative difference of approximately 0.29%. This indicates satisfactory convergence of the global voltage prediction at the evaluated operating point and supports the selection of M3 as a practical compromise between numerical accuracy and computational cost. Nevertheless, this comparison does not independently establish mesh convergence across the entire polarization curve or for local

temperature, oxygen concentration, and current-density distributions, which require separate spatial sensitivity assessments.

The resulting dataset provides the basis for the subsequent environmental-resilience analysis. In particular, the combined temperature and relative-humidity simulations enable the construction of two-dimensional and three-dimensional response maps, identification of dehydration- and flooding-dominated regimes, determination of critical environmental thresholds, and characterization of the operating region in which electrochemical performance, membrane hydration, oxygen accessibility, and thermal stability can be simultaneously maintained. These results are subsequently used to assess the resilience of PEMFC-based sustainable hydrogen power systems under increasingly demanding environmental conditions.

3. Results and Discussion

The results presented in this section evaluate the environmental resilience of the PEM fuel cell under the combined influence of temperature and relative-humidity extremes. Attention is given to the coupled effects of these environmental variables on electrochemical performance, membrane hydration, oxygen transport, liquid-water behavior, thermal distribution, and current-density uniformity. Rather than considering temperature and humidity as independent operating parameters, the analysis focuses on their interaction and on the transition between dehydration-dominated, balanced, and flooding-dominated operating regimes. The discussion therefore combines global performance indicators, including cell voltage and power density, with spatially resolved multiphysics parameters to identify the physical mechanisms responsible for performance enhancement or deterioration under each environmental condition. The results are further interpreted from a climate-resilience perspective to determine the operating regions in which the PEMFC maintains stable transport behavior and electrochemical output despite environmental stress. This approach provides the basis for constructing temperature–humidity response maps, defining critical environmental thresholds, and identifying operating conditions that support reliable and sustainable hydrogen power generation under increasingly variable climatic conditions.

Figure 2 presents the polarization response of the PEMFC under five representative temperature–humidity conditions selected to capture the principal environmental extremes investigated in this study. For all cases, cell voltage decreases progressively with increasing current density as the dominant losses shift from activation effects at low current densities toward increasingly significant ohmic and mass-transport limitations at higher loads. The relatively small separation between the curves in the low-current-density region indicates limited sensitivity to environmental conditions when reactant consumption and water production remain low. However, the curves progressively diverge as current density increases, demonstrating the growing influence of temperature and humidity on membrane hydration, proton conductivity, electrochemical kinetics, and reactant transport. The reference condition C11 (60 °C, 80% RH) provides the most favorable response over most of the investigated range, reflecting an effective balance between membrane hydration, reaction kinetics, and water removal. The hot–saturated condition C16 (80 °C, 100% RH) also maintains comparatively strong performance, whereas the cold–saturated case C4 (20 °C, 100% RH) exhibits greater voltage losses due to the combined influence of slower electrochemical kinetics and increased susceptibility to water accumulation.

The strongest performance deterioration occurs under the hot–dry condition C13 (80 °C, 20% RH), particularly at intermediate and high current densities. Elevated temperature combined with insufficient humidification promotes membrane dehydration, reducing proton conductivity and increasing ohmic resistance. The cold–dry case C1

(20 °C, 20% RH) similarly exhibits substantial losses, although these arise from the combined effects of insufficient membrane hydration and slower electrochemical kinetics. The increasing separation among the curves at high current density further demonstrates that environmental stress becomes particularly important during high-power operation, where reactant demand, electrochemical water production, heat generation, and mass-transfer resistance intensify simultaneously. These results confirm that PEMFC environmental resilience cannot be achieved by maximizing temperature or humidity independently; rather, reliable performance requires a balanced thermal–water-management condition capable of maintaining adequate membrane hydration while avoiding excessive water accumulation and associated oxygen-transport limitations.

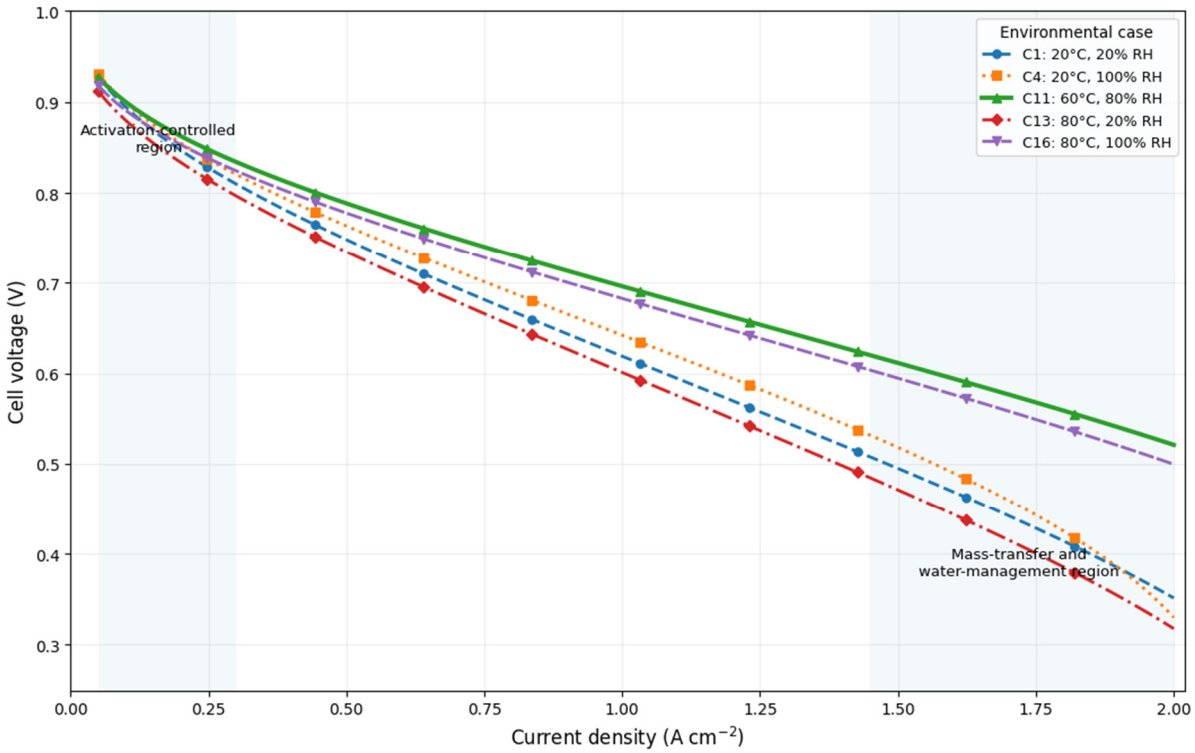


Figure 2. PEMFC polarization characteristics under representative temperature–relative-humidity conditions, illustrating the response to cold–dry (C1: 20 °C, 20% RH), cold–saturated (C4: 20 °C, 100% RH), reference (C11: 60 °C, 80% RH), hot–dry (C13: 80 °C, 20% RH), and hot–saturated (C16: 80 °C, 100% RH) environmental conditions.

Figure 3 illustrates the coupled evolution of cell voltage, power density, average membrane water content, and minimum oxygen concentration with increasing current density under the reference environmental condition C11 (60 °C and 80% RH). Cell voltage decreases continuously from approximately 0.93 V at low load to about 0.52 V at 2.0 A cm^{-2} as activation, ohmic, and mass-transport losses progressively increase. In contrast, power density rises with current density and reaches approximately 1.04 W cm^{-2} at the upper end of the investigated range, demonstrating that the increasing electrical load compensates for the progressive voltage reduction. Membrane water content simultaneously increases from approximately 11.5 at low current density to a maximum of about 14.4 near 1.5 A cm^{-2}. This increase results from greater electrochemical water production and enhanced membrane hydration as the reaction rate increases. Beyond this region, a moderate decline in membrane water content is observed, indicating that water removal and transport become increasingly competitive with local water generation at elevated current density.

The oxygen-transport response exhibits an opposite trend, with the minimum cathode oxygen concentration decreasing continuously from approximately 7.1 to nearly 1.0 mol m^{-3} as current density approaches 2.0 A cm^{-2}. This pronounced depletion reflects the rapidly increasing oxygen consumption associated with the oxygen reduction reaction and indicates the progressive development of cathode mass-transfer limitations at high electrical loads. The simultaneous increase in membrane hydration and reduction in oxygen availability highlights the coupled nature of PEMFC water and reactant management: improved hydration supports proton conduction, but increasing water production and reactant consumption can eventually restrict oxygen accessibility within the porous cathode structure. The results therefore demonstrate why the reference environmental condition provides favorable operation across a broad load range while also revealing the onset of transport constraints at high current density. This coupled electrochemical–hydration–transport behavior provides an important baseline for evaluating how temperature and humidity extremes alter the internal resilience of the cell in the subsequent analyses.

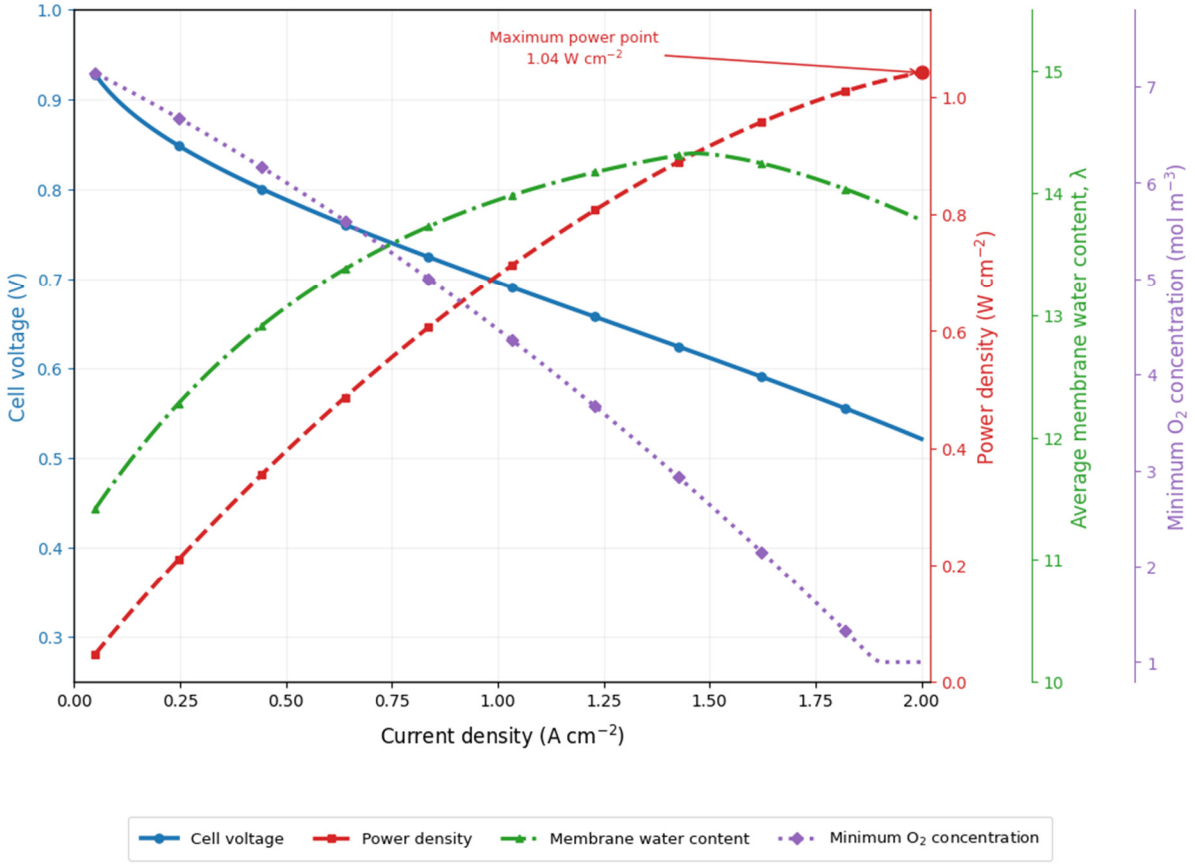


Figure 3. Coupled variation in cell voltage, power density, average membrane water content, and minimum cathode oxygen concentration with current density under the reference environmental condition C11 (60 °C and 80% RH), illustrating the interaction between electrochemical performance, membrane hydration, and oxygen-transport limitations.

Figure 4 compares the contributions of activation, ohmic, and mass-transfer losses at a representative high-load operating condition of 1.5 A cm^{-2} for the selected environmental scenarios. A clear redistribution of the dominant loss mechanisms is observed as temperature and relative humidity change. The reference case C11 (60 °C, 80% RH) exhibits the lowest total voltage loss, approximately 0.320 V, with relatively limited contributions from all three loss components. In contrast, the cold–dry C1 and hot–dry

C13 conditions produce substantially larger total losses of approximately 0.458 and 0.457 V, respectively. Despite their similar total losses, their physical origins are not identical. C13 exhibits the largest ohmic contribution, accounting for more than half of the total loss, which is consistent with intensified membrane dehydration at elevated temperature and low humidity. Under C1, the combined effects of insufficient hydration, reduced electrochemical kinetics, and transport resistance produce a more distributed loss profile.

Humidity also produces a distinct influence on the relative importance of the different loss mechanisms. Increasing RH from the dry C1 condition to the saturated C4 condition reduces the ohmic contribution through improved membrane hydration; however, the mass-transfer component becomes more pronounced under the cold–saturated environment. This behavior indicates that increasing humidification can shift the dominant limitation from proton conduction toward reactant transport as water accumulation becomes increasingly significant within the cathode porous structure. Conversely, C16 (80 °C, 100% RH) maintains comparatively low activation and mass-transfer losses, suggesting that the higher temperature facilitates reaction kinetics and water removal while sufficient humidity preserves membrane hydration. The loss decomposition therefore reinforces an important aspect of PEMFC environmental resilience: similar overall performance deterioration can originate from fundamentally different mechanisms, and an environmentally robust operating condition requires simultaneous control of membrane hydration, electrochemical kinetics, and reactant transport rather than optimization of temperature or humidity independently.

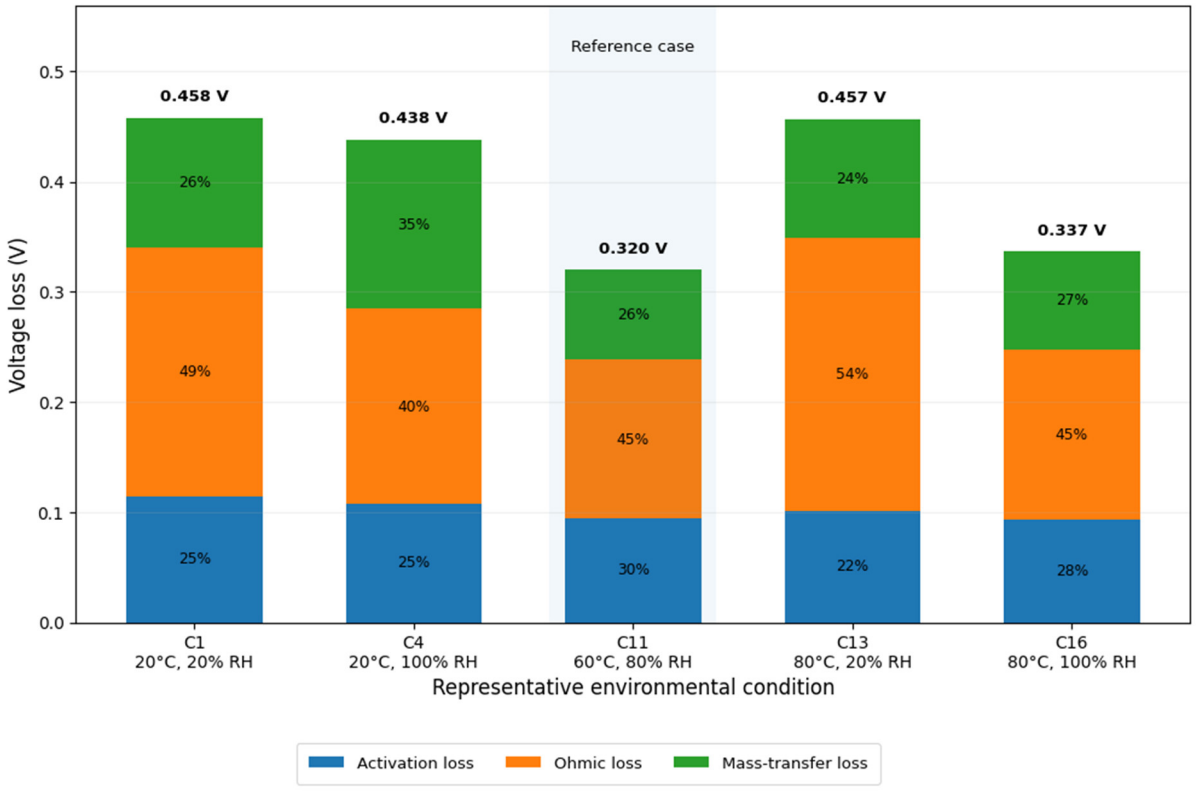


Figure 4. Decomposition of activation, ohmic, and mass-transfer voltage losses at a current density of 1.5 A cm^{-2} under representative temperature–relative-humidity conditions, showing the redistribution of dominant electrochemical and transport losses between cold–dry (C1), cold–saturated (C4), reference (C11), hot–dry (C13), and hot–saturated (C16) environmental scenarios.

Figure 5 compares the temperature non-uniformity (ΔT) and current-density non-uniformity (CV_j) under the five representative environmental conditions, providing a

spatial assessment of PEMFC resilience beyond the global electrochemical performance discussed previously. Considerable differences are observed among the investigated cases, demonstrating that temperature and relative humidity influence not only the magnitude of cell performance but also its spatial distribution. The reference condition C11 (60 °C, 80% RH) exhibits the lowest temperature difference of approximately 2.2 K and the lowest current-density coefficient of variation of 7.4%. These values indicate comparatively homogeneous heat generation and electrochemical activity across the active area, supporting the favorable thermal–hydration balance identified for this condition in the preceding analyses.

Environmental extremes substantially increase spatial non-uniformity, with the strongest deterioration occurring under the hot–dry condition C13 (80 °C, 20% RH). The temperature difference increases to approximately 5.4 K, while CV_j reaches 21.2%, nearly three times the value obtained for C11. This pronounced non-uniformity can be associated with spatially uneven membrane dehydration, which modifies local proton conductivity and consequently redistributes electrochemical reaction activity across the cell. The cold–dry C1 condition also produces relatively high current-density non-uniformity of 15.8%, accompanied by a temperature difference of 3.1 K. Increasing humidity at 20 °C, represented by C4, moderately improves both parameters; however, CV_j remains considerably higher than under the reference condition, indicating that adequate humidification alone cannot completely compensate for the adverse influence of low operating temperature.

The hot–saturated condition C16 demonstrates an important intermediate behavior. Despite operating at the same temperature as C13, increasing RH from 20% to 100% reduces the current-density non-uniformity from 21.2% to 10.1% and decreases ΔT from 5.4 to 3.8 K. This substantial improvement demonstrates the critical role of membrane hydration in suppressing localized electrochemical and thermal gradients under elevated-temperature operation. Nevertheless, the remaining thermal non-uniformity relative to C11 indicates that excessive temperature cannot be fully compensated by humidification. From an environmental-resilience perspective, these findings demonstrate that maintaining global voltage or power output alone is insufficient for identifying robust PEMFC operating conditions. Minimizing spatial thermal and current-density gradients is equally important because persistent, localized stresses may accelerate material degradation and reduce long-term durability. The superior uniformity observed for C11 therefore further supports the existence of a balanced temperature–humidity operating region in which thermal management, membrane hydration, and electrochemical activity are simultaneously stabilized.

Figure 6 illustrates the coupled relationship between average membrane water content, minimum cathode oxygen concentration, and liquid-water saturation across the investigated temperature–humidity conditions. A clear shift in the internal transport state is observed as relative humidity increases. At low RH, the membrane water content remains comparatively low, particularly at elevated temperatures, while the minimum oxygen concentration is relatively high because limited liquid-water accumulation preserves gas-phase transport pathways within the cathode porous structure. Increasing RH progressively shifts the operating points toward higher membrane water content, confirming improved membrane hydration. However, this improvement is accompanied by a general reduction in minimum cathode oxygen concentration and an increase in marker size, representing greater liquid-water saturation. The results therefore demonstrate an important trade-off between maintaining sufficient membrane hydration for proton conduction and preserving adequate pore accessibility for oxygen transport.

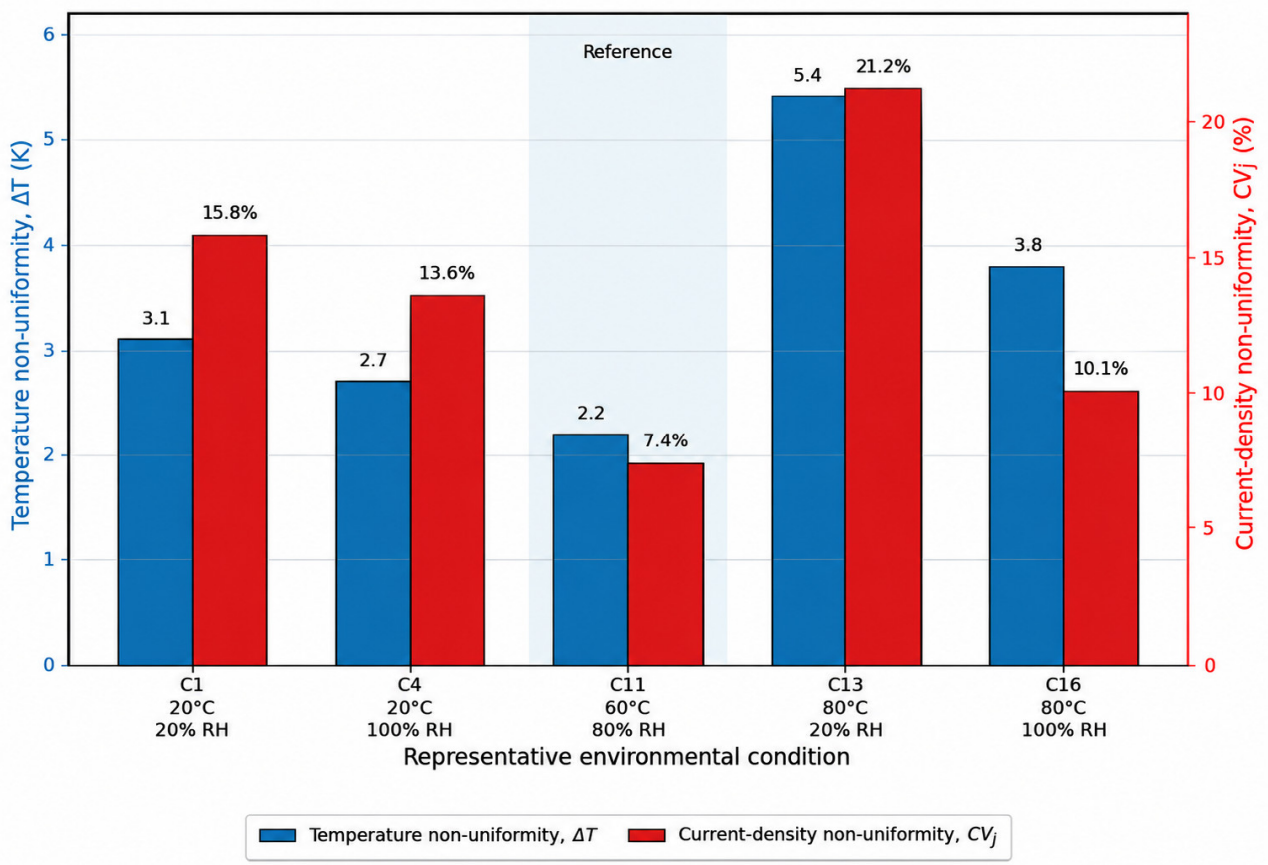


Figure 5. Temperature non-uniformity (ΔT) and current-density non-uniformity (CV_j) under representative temperature–relative-humidity environmental conditions, demonstrating the influence of coupled thermal and humidity stresses on the spatial stability of PEMFC operation.

The influence of temperature becomes particularly evident when conditions with similar relative humidity are compared. Under dry operation, the hot condition at 80 °C produces the lowest membrane water content, indicating pronounced susceptibility to membrane dehydration despite relatively favorable oxygen availability. Conversely, increasing humidity substantially restores membrane hydration at elevated temperature while maintaining comparatively better oxygen accessibility than under equivalent low-temperature, highly humid conditions. At 100% RH, for example, the lower-temperature cases exhibit larger liquid-water saturation and stronger oxygen depletion, indicating an increased tendency toward cathode flooding. This behavior can be attributed to the reduced water-vapor carrying capacity at lower temperature, which favors condensation and liquid-water retention. Elevated temperature facilitates water evaporation and removal, but when combined with insufficient humidity it shifts the limiting mechanism in the opposite direction toward membrane dehydration. Thus, temperature determines whether increasing or decreasing humidity predominantly affects ionic conduction or gas-phase mass transport.

The reference condition C11 (60 °C, 80% RH) occupies a comparatively favorable region of the hydration–oxygen transport space, combining a membrane water content of approximately 14.3 with a minimum oxygen concentration of about 4.6 mol m^{-3} while maintaining relatively limited liquid-water saturation. This position illustrates the balance required for environmentally resilient PEMFC operation: sufficient water must be retained to support high proton conductivity without producing excessive liquid-water accumulation that obstructs oxygen transport. The overall distribution of the environmental cases consequently reveals two competing failure tendencies, namely

dehydration under hot–dry conditions and oxygen-transport deterioration under highly humid, particularly lower-temperature conditions. These findings reinforce the need to consider temperature and humidity as coupled environmental stresses rather than independent variables when defining robust operating windows for PEMFC-based hydrogen power systems.

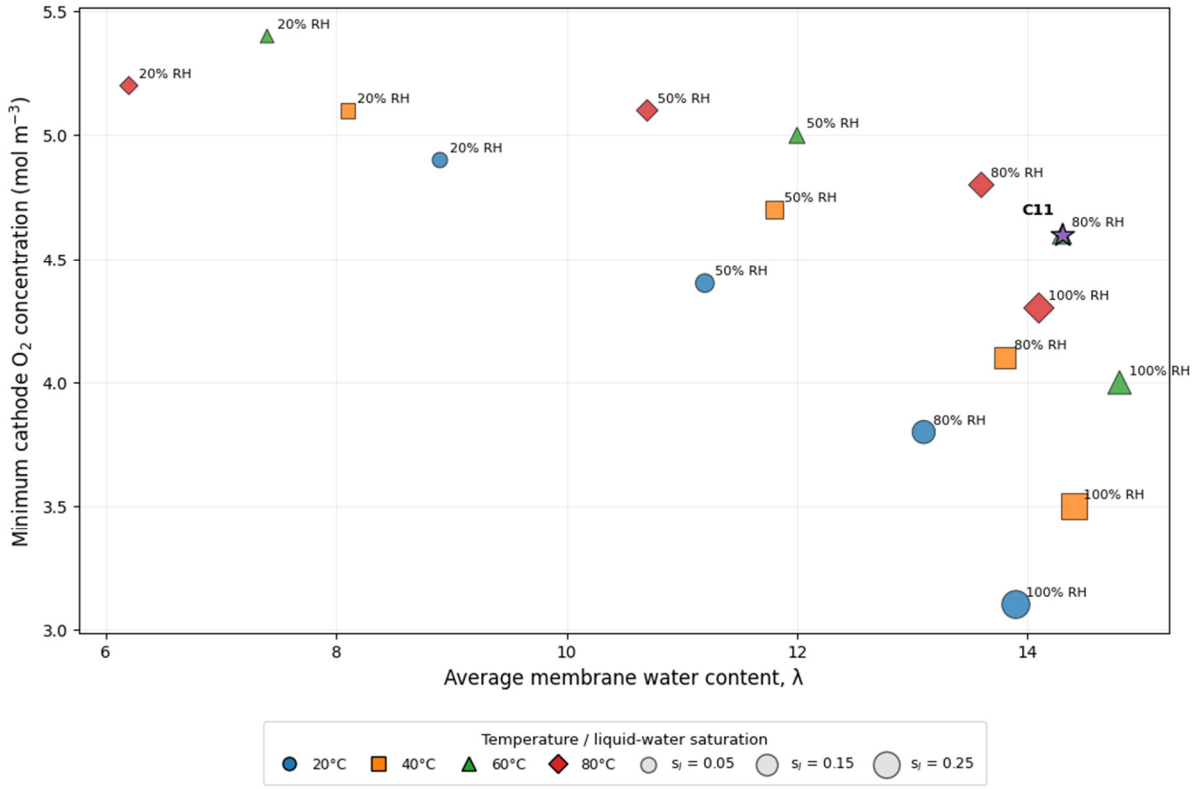


Figure 6. Coupled relationship between average membrane water content and minimum cathode oxygen concentration across the investigated temperature–relative-humidity conditions, with marker size representing liquid-water saturation. The distribution illustrates the transition between dehydration-dominated and water-accumulation-/oxygen-transport-limited operating regimes, with C11 (60 °C, 80% RH) highlighted as the reference condition.

Figure 7 presents the spatial distribution of local membrane water content (λ) across the active area under four representative environmental conditions at moderate (0.5 A cm^{-2}) and high (1.5 A cm^{-2}) current densities. At moderate load, the distributions are relatively narrow, indicating comparatively uniform membrane hydration within each environmental case. Nevertheless, substantial shifts in the distribution centers are evident. The hot–dry condition C13 (80 °C, 20% RH) is concentrated around the lowest λ values, reflecting pronounced membrane dehydration, while C1 (20 °C, 20% RH) exhibits a moderately higher hydration level. In contrast, the highly humid C4 and reference C11 conditions are concentrated around $\lambda \approx 13.5$–14.0, demonstrating substantially improved membrane hydration. C11 additionally exhibits the narrowest distribution, suggesting that 60 °C and 80% RH provide not only favorable average hydration but also a comparatively homogeneous water distribution across the membrane.

Increasing the current density to 1.5 A cm^{-2} noticeably broadens the distributions, particularly for the dry environmental cases, demonstrating that high electrical loading intensifies spatial hydration heterogeneity. C13 undergoes the strongest shift toward lower λ values and develops a substantially broader distribution, indicating that elevated temperature combined with low inlet humidity promotes localized membrane drying as

electro-osmotic water transport and thermal effects intensify. C1 also exhibits greater dispersion at high load, although its hydration state remains less severely depleted than C13. Conversely, C4 and C11 remain concentrated within the high-hydration region despite some broadening, with C11 retaining a comparatively narrow distribution around $\lambda \approx 14.4$. These results demonstrate that environmental resilience cannot be characterized adequately using average membrane water content alone; the spatial distribution and variability of hydration are equally important because localized dry regions can increase protonic resistance and promote non-uniform electrochemical activity even when the domain-averaged hydration remains acceptable.

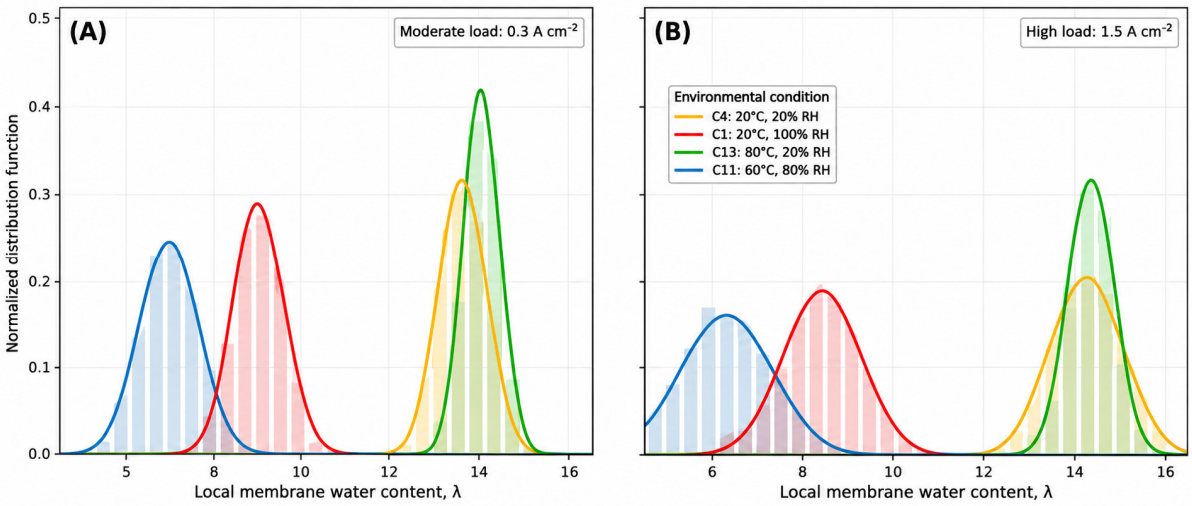


Figure 7. Normalized spatial distributions of local membrane water content (λ) across the PEMFC active area under representative environmental conditions at (**A**) moderate load of 0.5 A cm^{-2} and (**B**) high load of 1.5 A cm^{-2}. The distributions illustrate the effects of temperature, relative humidity, and electrical loading on membrane hydration level and spatial uniformity, highlighting increased dehydration and hydration heterogeneity under hot–dry conditions.

To complement the normalized statistical distributions of membrane water content presented in Figure 7, Figure 8 provides a schematic visualization of the spatial variations in temperature, current density, oxygen concentration, membrane water content, and liquid-water saturation under two contrasting environmental conditions: C11 (60 °C, 80% RH) and C13 (80 °C, 20% RH). These conditions represent favorable and hot–dry operating regimes, respectively. The comparison illustrates the expected physical differences between the two environments, including more favorable membrane hydration and electrochemical uniformity under C11 and increased dehydration, thermal gradients, and transport limitations under C13. Furthermore, the representation highlights the relationship between local electrochemical activity, oxygen availability, membrane hydration, and water accumulation within the PEMFC. Unlike the statistical distributions in Figure 6, which describe the frequency and variability of membrane hydration values, the schematic in Figure 8 illustrates how these coupled physical phenomena may vary across the cell geometry. This complementary representation facilitates the interpretation of spatial non-uniformities while providing a conceptual connection between the multiphysics model and the environmental-resilience indicators discussed throughout the study.

The Environmental Resilience Index (ERI), defined in Equation (38), provides an integrated assessment of the combined effects of temperature and relative humidity on electrochemical performance, membrane hydration, oxygen transport, and current-density uniformity. The equal-weight formulation enables systematic comparison of the

investigated environmental scenarios without prioritizing a particular physical mechanism. The individual indicators reveal that the reference condition C11 (60 °C, 80% RH) provides a favorable balance between membrane hydration, electrochemical performance, and spatial uniformity, whereas the hot–dry condition C13 (80 °C, 20% RH) exhibits substantial deterioration associated with dehydration and increased transport resistance. The composite ERI should therefore be interpreted alongside its constituent indicators to distinguish the mechanisms responsible for environmental performance differences.

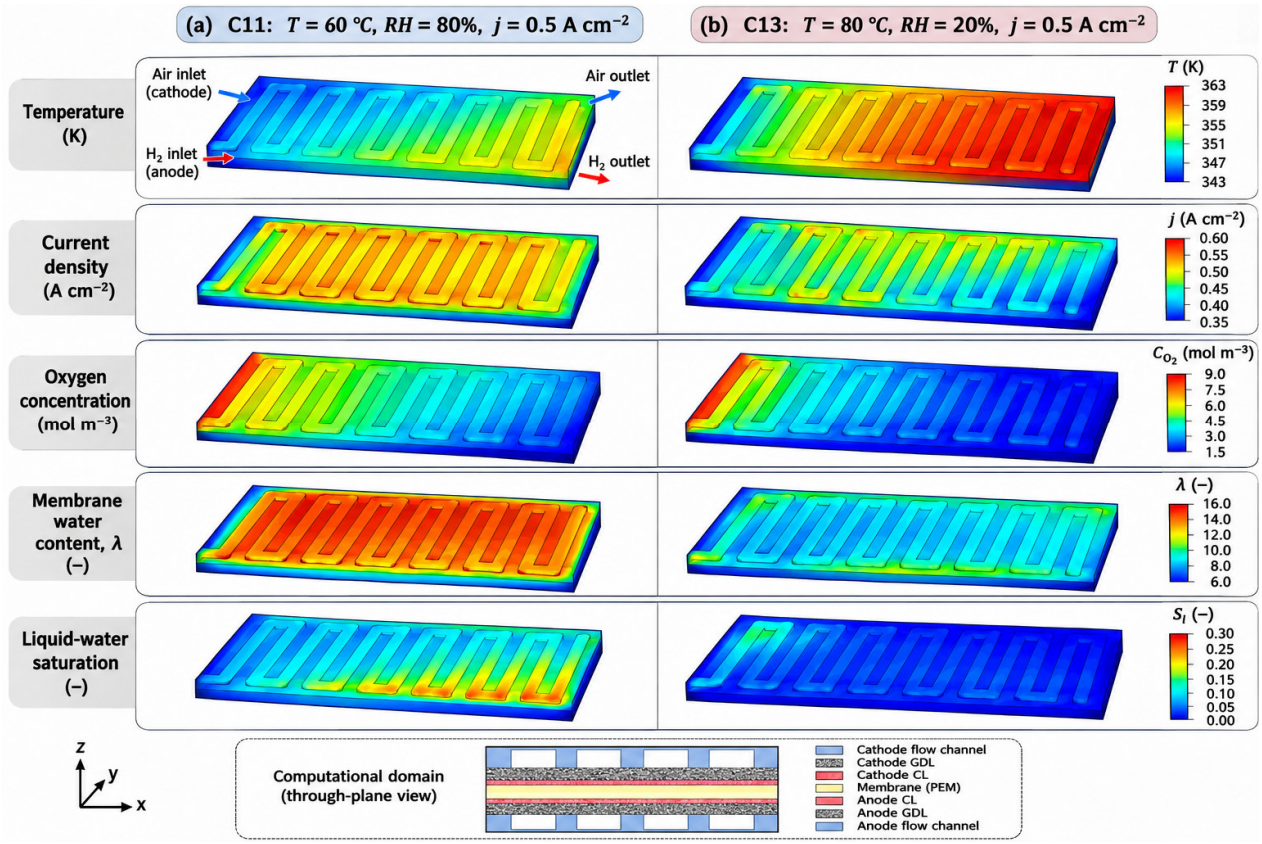


Figure 8. Illustrative three-dimensional spatial-field comparison of a proton exchange membrane fuel cell under two contrasting environmental conditions: (**a**) C11 (60 °C, 80% RH) and (**b**) C13 (80 °C, 20% RH). The panels schematically represent temperature, local current density, oxygen concentration, membrane water content, and liquid-water saturation, together with the through-plane arrangement of the principal PEMFC components. The visualization is conceptual and does not represent numerical contour data extracted from the CFD simulations.

Figure 9 presents the variation in cathode oxygen utilization across the complete set of 16 environmental scenarios, providing a quantitative measure of how effectively the supplied oxygen participates in the electrochemical reaction under combined temperature and humidity stresses. At each temperature level, oxygen utilization generally increases as relative humidity rises from 20% toward 80% RH. At 20 °C, for example, utilization increases from approximately 56.8% for C1 to 66.9% for C3, while at 40 °C it increases from 60.4% for C5 to 73.8% for C7. This improvement can be associated with progressively better membrane hydration and proton transport, which support more effective electrochemical reaction and consequently increase oxygen consumption. However, increasing RH further to 100% produces a moderate decline at both temperatures, indicating that maximum humidification does not necessarily correspond to maximum oxygen utilization.

The most favorable response occurs within the 60 °C group, where oxygen utilization increases from 62.1% for C9 to a maximum of approximately 79.4% for the reference condition C11 (60 °C, 80% RH), before decreasing to 75.1% for the fully saturated C12 condition. This non-monotonic dependence on humidity is important because it reveals the competing effects of hydration and cathode water accumulation. Increasing RH initially improves membrane hydration and facilitates electrochemical activity; beyond an optimum range, however, additional water can progressively occupy pore space within the cathode catalyst layer and gas-diffusion medium, restricting effective oxygen delivery to active reaction sites. The maximum observed around C11 is therefore consistent with a balanced water-management condition in which sufficient membrane hydration is achieved without imposing excessive oxygen-transport resistance.

The 80 °C scenarios further demonstrate the strong coupling between thermal and humidity stresses. Under the hot–dry C13 condition, oxygen utilization decreases to approximately 51.7%, the lowest value among the investigated cases, whereas increasing RH to 50% and 80% raises utilization to approximately 67.8% and 76.3%, respectively. The recovery indicates that adequate humidification becomes increasingly important at elevated temperature because it counteracts membrane dehydration and supports more spatially distributed electrochemical activity. Nevertheless, utilization again decreases slightly at 100% RH (C16), confirming that excessive humidification can introduce transport penalties even at elevated temperature. Collectively, the 16 scenarios demonstrate that cathode oxygen utilization is governed by the coupled influence of temperature and humidity rather than either environmental variable independently, with the intermediate-to-high humidity range-particularly around C11-providing the most favorable balance between membrane hydration and oxygen accessibility.

To complement the statistical membrane-hydration distributions presented in Figure 6, representative spatial contour fields are considered for C11 (60 °C, 80% RH) and C13 (80 °C, 20% RH). These operating conditions represent contrasting electrochemical and water-management regimes. The spatial comparison is intended to distinguish the locations of thermal gradients, current-density non-uniformity, oxygen depletion, membrane dehydration, and liquid-water accumulation, which cannot be identified from normalized statistical distributions alone. In particular, the previously reported differences in current-density and temperature non-uniformity between C11 and C13 indicate that the hot–dry condition is associated with a less homogeneous electrochemical and thermal response. The combined interpretation of statistical distributions and local contour fields therefore provides a more complete assessment of spatial resilience under changing temperature and humidity conditions.

Figure 10 presents the influence of combined temperature and relative-humidity conditions on cathode flow-channel pressure drop and the associated air-pumping power penalty at a representative current density of 1.5 A cm^{-2}. A systematic increase in pressure drop is observed with increasing relative humidity at each investigated temperature. At 20 °C, ΔP increases from approximately 121 Pa for C1 (20% RH) to 168 Pa for C4 (100% RH), accompanied by an increase in pumping-power penalty from 1.92% to 2.72% of the gross power. A similar humidity-dependent trend occurs at 40, 60, and 80 °C, although the absolute pressure drop progressively decreases as temperature increases. This behavior can be attributed primarily to changes in cathode water management: under highly humid and lower-temperature conditions, enhanced liquid-water accumulation within the flow channel and porous transport regions increases resistance to gas flow, thereby requiring greater auxiliary power to maintain the prescribed reactant supply.

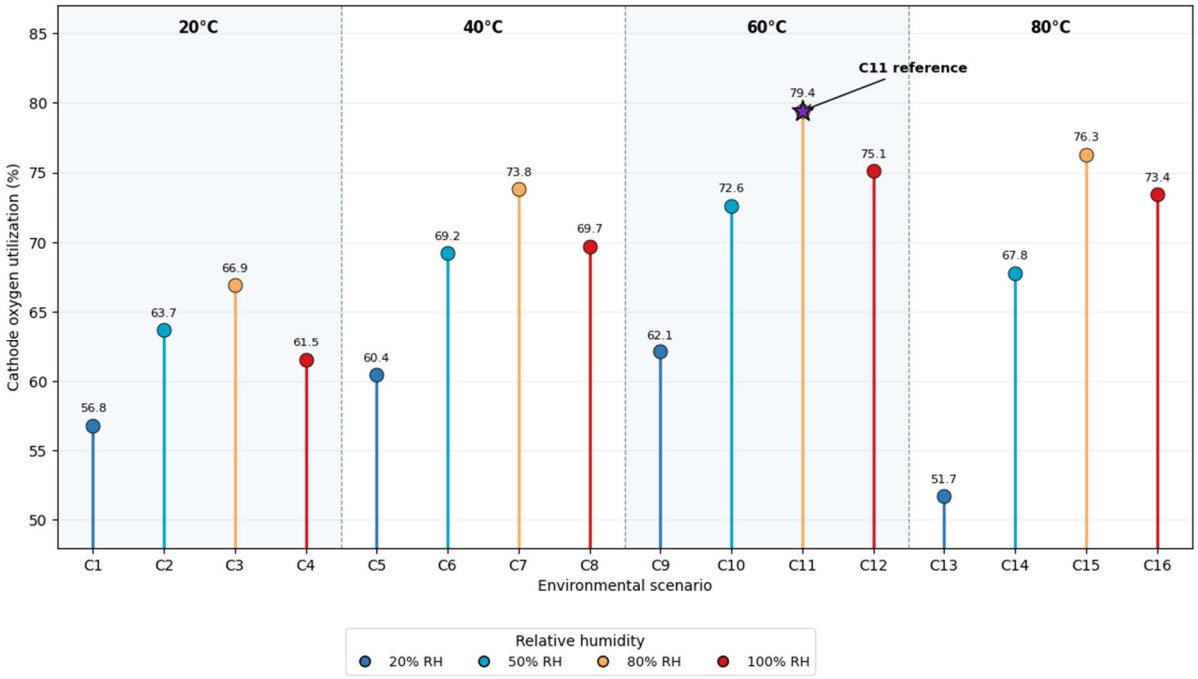


Figure 9. Cathode oxygen utilization across the 16 temperature–relative-humidity environmental scenarios at the representative operating current density of 1.5 A cm^{-2}. The scenarios are grouped by operating temperature (20, 40, 60, and 80 °C), while marker colors distinguish relative humidity levels of 20, 50, 80, and 100% RH; C11 (60 °C, 80% RH) represents the reference condition and exhibits the highest oxygen utilization among the investigated cases.

Temperature considerably moderates this fluid-dynamic penalty. At 80 °C, the pressure drop varies from approximately 97 Pa for the dry C13 condition to 126 Pa for the saturated C16 condition, while the corresponding pumping-power penalty remains between approximately 1.36% and 1.76%. The reference case C11 (60 °C, 80% RH) exhibits an intermediate pressure drop of approximately 119 Pa and a pumping-power penalty of 1.69%, indicating a favorable compromise between adequate humidification and manageable cathode flow resistance. Importantly, these results reveal an additional trade-off in environmental PEMFC operation: increasing humidity can improve membrane hydration and electrochemical performance, as demonstrated in the preceding analyses, but excessive humidification may simultaneously increase hydraulic resistance and parasitic energy consumption. Consequently, environmental resilience should be assessed not only from gross electrochemical output but also from the auxiliary energy required to sustain reactant delivery under changing temperature and humidity conditions.

Figure 11 presents the maximum admissible current density that can be sustained under the 16 investigated temperature–humidity scenarios while simultaneously maintaining the prescribed electrochemical and transport constraints. A strong dependence on relative humidity is observed across all temperature levels. Under dry conditions (20% RH), the admissible current density remains comparatively limited, ranging from 0.74 A cm^{-2} at 80 °C (C13) to 1.10 A cm^{-2} at 60 °C (C9), and none of these conditions reaches the target operating load of 1.50 A cm^{-2}. Increasing RH to 50% substantially expands the allowable operating range, particularly at 40 and 60 °C, where C6 and C10 reach approximately 1.52 and 1.66 A cm^{-2}, respectively. The improvement becomes more pronounced at 80% RH, where C7, C11, and C15 can sustain approximately 1.76, 1.98, and 1.71 A cm^{-2}. These results demonstrate that insufficient humidification restricts the usable current-density envelope because membrane dehydration and the

associated increase in proton-transport resistance become increasingly important as electrical loading rises.

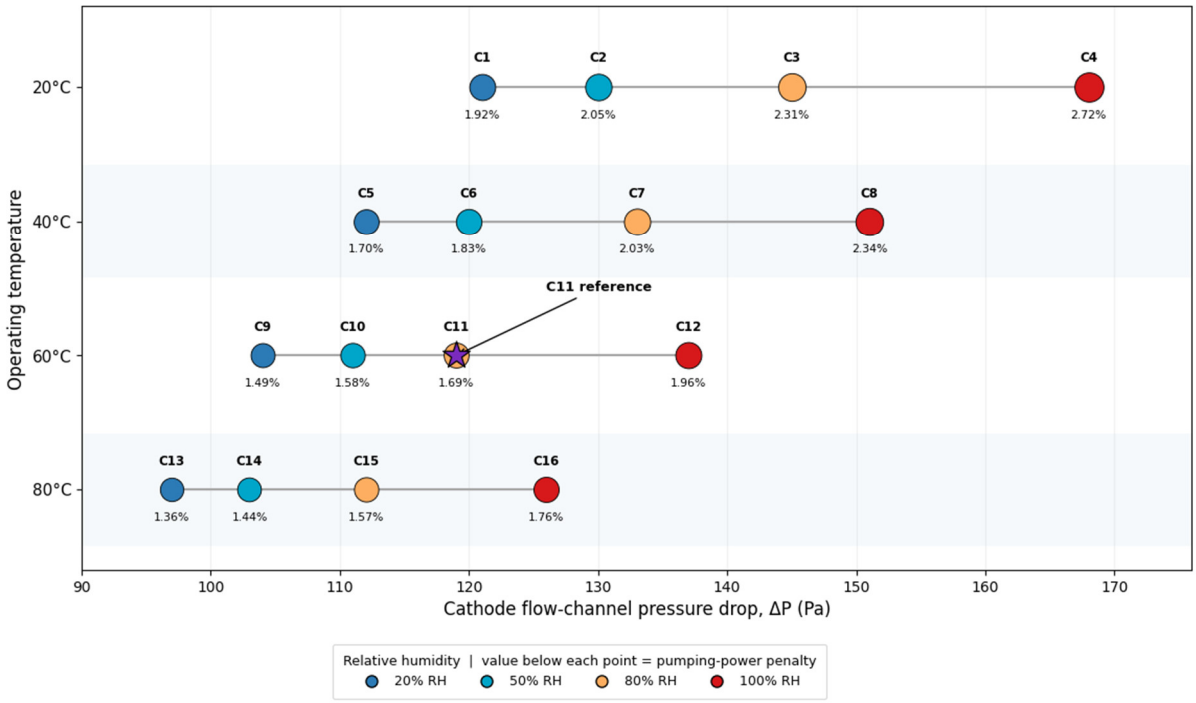


Figure 10. Cathode flow-channel pressure drops and associated air-pumping power penalty for the 16 temperature–relative-humidity environmental scenarios at a current density of 1.5 A cm^{-2}. Cases are grouped according to operating temperature (20, 40, 60, and 80 °C), with marker colors representing relative humidity levels of 20, 50, 80, and 100% RH; the percentages below the markers indicate the corresponding pumping-power penalty relative to gross cell power.

The most favorable operating envelope is obtained for C11 (60 °C, 80% RH), which reaches a maximum admissible current density of approximately 1.98 A cm^{-2}, substantially exceeding the 1.50 A cm^{-2} target. Increasing humidity further to 100% does not provide an additional improvement; instead, the admissible current density decreases moderately at each temperature, including a reduction from 1.98 to 1.82 A cm^{-2} between C11 and C12 at 60 °C. This behavior reflects the competing requirements of membrane hydration and reactant transport: moderate-to-high humidity supports ionic conduction, whereas excessive humidification increasingly promotes water accumulation and oxygen-transport limitations. The particularly low value obtained for the hot–dry C13 condition further demonstrates the vulnerability of PEMFC operation to simultaneous high-temperature and low-humidity exposure. Consequently, the admissible-current envelope provides an integrated measure of environmental resilience by identifying not merely the condition producing the highest instantaneous performance, but the combinations of temperature and humidity under which the cell can safely sustain demanding electrical loads without violating critical hydration, voltage, and reactant-transport limits.

Figure 12 provides an integrated assessment of the system-level consequences of combined temperature and humidity variations by simultaneously examining net power density, thermal efficiency, hydrogen consumption rate, and specific CO_2 emissions across the 16 environmental scenarios. As shown in Figure 12a, net power density varies considerably with the imposed environmental conditions, demonstrating that the electrical output of the PEMFC system is strongly dependent on the interaction between thermal state and reactant humidification. Within each temperature group, increasing relative humidity from the dry condition generally improves net power density until an

intermediate-to-high humidity range is reached, after which the improvement diminishes or reverses. To ensure numerical consistency between the electrochemical polarization characteristics and the system-level power assessment, the gross and net power densities were evaluated using the same operating voltage and current density. Gross power density was calculated as the product of cell voltage and current density, whereas net power density was determined after subtracting the auxiliary air-pumping power normalized by the active cell area. For the reference condition C11 (60 °C and 80% RH), the polarization results indicate a cell voltage of approximately 0.52 V at 2.0 A cm^{-2}, corresponding to a gross power density of 1.04 W cm^{-2}. Consequently, the corresponding net power density must remain below this value after accounting for auxiliary consumption. This verification establishes a consistent physical relationship between the polarization results and the system-level power calculations. The net power density values should therefore be reported using the corresponding electrical operating points and pumping requirements, ensuring that auxiliary losses are consistently incorporated across all investigated environmental scenarios. The pronounced deterioration under C13 confirms that simultaneous exposure to elevated temperature and insufficient humidity represents one of the most critical environmental combinations because membrane dehydration and increased protonic resistance restrict the achievable electrochemical output.

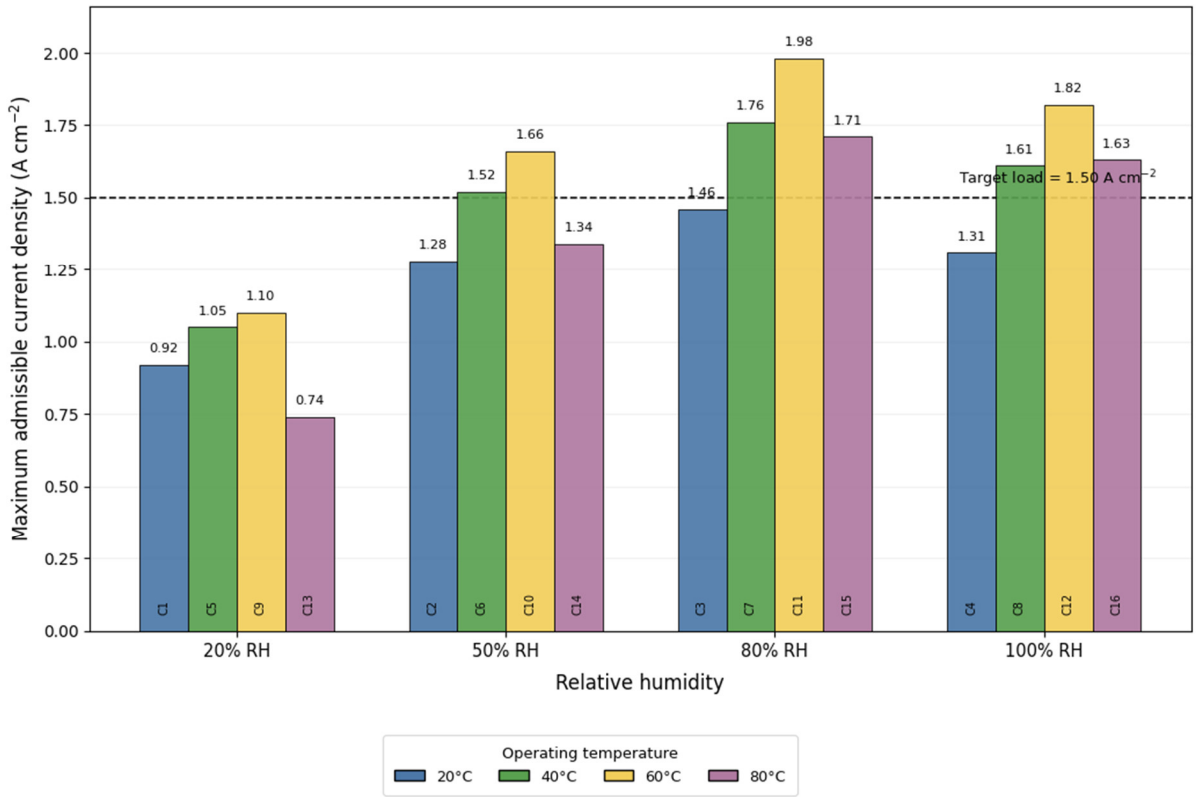


Figure 11. Maximum admissible current density under the 16 investigated temperature–relative-humidity scenarios based on simultaneous electrochemical and transport constraints. The dashed horizontal line denotes the target operating current density of 1.50 A cm^{-2}, while the four bar colors represent operating temperatures of 20, 40, 60, and 80 °C. The results identify the environmentally robust operating envelope and demonstrate the maximum sustainable loading under combined temperature and humidity stresses.

To ensure consistency between the polarization characteristics and the calculated power output, the gross power density is determined as $P_{gross} = V \times j$, while the net power

density is calculated by subtracting the auxiliary power consumption normalized by the active cell area. For the reference condition C11, the cell voltage of approximately 0.52 V at 2.0 A cm^{-2} corresponds to a gross power density of 1.04 W cm^{-2}. Accordingly, the net power density at this operating point must be equal to or lower than 1.04 W cm^{-2}, depending on the associated auxiliary power requirements. This distinction ensures consistency between the polarization results, power calculations, and the physical energy balance of the PEMFC system.

The thermal-efficiency behavior presented in Figure 12b further demonstrates the sensitivity of energy conversion to the environmental operating state. Across the investigated scenarios, the efficiency generally improves as the system approaches adequately humidified conditions and reaches its most favorable range around the intermediate temperature–humidity combinations. The 60 °C cases consistently exhibit comparatively high thermal efficiency, with C11 representing the most favorable condition within the investigated matrix. In contrast, the 80 °C group shows substantially lower efficiency, particularly under dry operation, indicating that elevated temperature alone does not guarantee improved system performance when membrane hydration cannot be maintained. The subsequent reduction observed when humidity increases from 80% to 100% also indicates that excessive humidification can offset part of the benefit obtained from improved ionic transport, as water accumulation introduces additional mass-transfer limitations. The thermal-efficiency response therefore reinforces the existence of an environmental optimum rather than a simple monotonic dependence on either temperature or humidity.

Figure 12c examines the corresponding hydrogen-consumption behavior and reveals how environmental conditions affect fuel demand in conjunction with the obtainable system output. Hydrogen consumption increases as electrochemical activity becomes stronger and reaches comparatively high values around the favorable intermediate-temperature and adequately humidified conditions. However, hydrogen consumption should not be interpreted independently as an indicator of superior performance, because the useful electrical output obtained from the consumed fuel must also be considered. The simultaneous increase in power density and favorable efficiency around C11 indicates that the increased hydrogen utilization in this region is accompanied by effective energy conversion. Conversely, environmentally stressed conditions can produce an unfavorable relationship between fuel utilization and useful net output. This result highlights the importance of evaluating hydrogen demand together with electrical and thermal performance when assessing the practical resilience of hydrogen-powered PEMFC systems under changing climatic conditions.

Figure 12b–d presents the responses of the 16 investigated operating scenarios, grouped according to their prescribed inlet temperatures. Each temperature group contains four relative-humidity conditions (20%, 50%, 80%, and 100%), corresponding to C1–C4 at 20 °C, C5–C8 at 40 °C, C9–C12 at 60 °C, and C13–C16 at 80 °C. Accordingly, each panel contains 16 distinct data points distributed across four temperature-dependent curves, ensuring consistency with the scenario matrix defined in Table 2. This representation facilitates direct comparison of humidity effects at fixed temperature without introducing additional operating scenarios.

The environmental implications of the investigated operating conditions should be interpreted in relation to the upstream carbon intensity of hydrogen supply and auxiliary-energy consumption rather than as direct CO_2 emissions from the PEMFC. Hydrogen-fuelled PEMFC operation does not generate CO_2 at the point of use; however, its overall carbon footprint depends on the hydrogen-production pathway, electricity source, transportation requirements, and selected system boundary. Consequently, variations in cell voltage, hydrogen utilization, and net electrical output can influence the upstream

emissions associated with each unit of useful electricity delivered. The favourable electrochemical performance observed under C11 (60 °C and 80% RH) may reduce the hydrogen-related carbon burden per unit of electricity compared with less favourable operating conditions, provided the same hydrogen-supply assumptions and operating-load basis are applied. Nevertheless, without a verified lifecycle inventory and documented upstream emission factors, absolute carbon-intensity values cannot be established reliably. The present findings therefore support a qualitative relationship between environmental operating conditions, fuel-cell efficiency, and potential upstream carbon impacts, rather than a definitive lifecycle-emission ranking. Future investigations should integrate pathway-specific hydrogen-production inventories, electricity-mix scenarios, and uncertainty analysis to quantify these environmental effects more comprehensively.

To ensure consistency between the cell-level and system-level performance assessments, gross and net power densities are distinguished explicitly. Gross power density is calculated as the product of cell voltage and current density ($P_{gross} = jV$), whereas net power density is obtained by subtracting the auxiliary pumping power per unit active area ($P_{net} = P_{gross} - P_{pump}/A$). Under the reference condition C11, Figure 3 indicates a gross power density of approximately 1.04 W cm^{-2} at 2.0 A cm^{-2}. Accordingly, the corresponding net power density must be lower than or equal to this value. The net-power results should therefore be evaluated at clearly identified operating points using the same electrical loading conditions and consistent auxiliary-power assumptions.

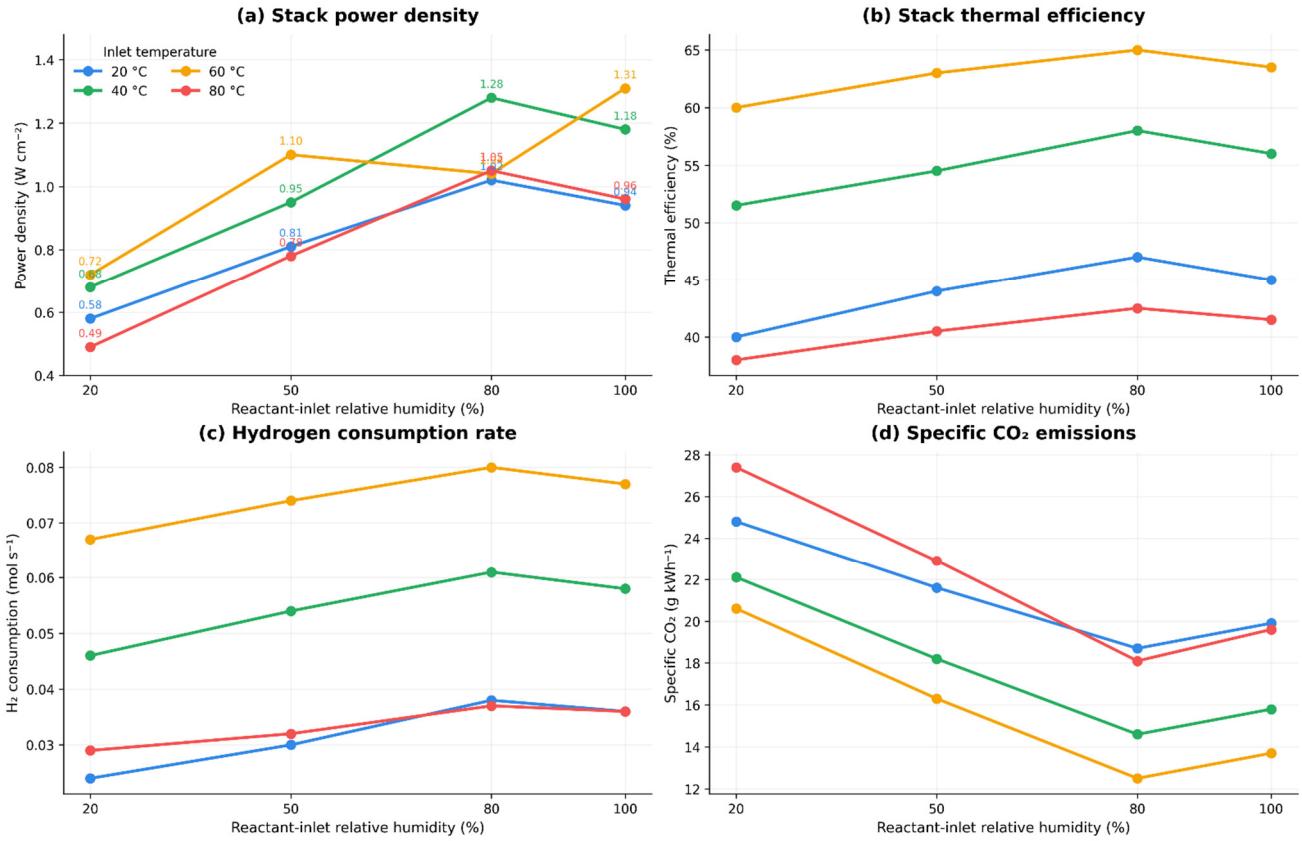


Figure 12. Effects of reactant-inlet temperature and relative humidity on PEMFC performance and environmental indicators: (**a**) net power density, (**b**) thermal efficiency, (**c**) hydrogen consumption rate, and (**d**) specific CO_2 emissions. The results represent 16 distinct operating scenarios (C1–C16), organized into four temperature groups (20, 40, 60, and 80 °C), each comprising four relative-humidity levels (20%, 50%, 80%, and 100%). Each curve contains four data points, ensuring consistency with the operating conditions defined in Table 2.

It should be emphasized that C11 (60 °C, 80% RH) represents the most favorable operating condition within the investigated discrete temperature–humidity matrix rather than a mathematically established global optimum. The present analysis considers 16 operating scenarios with temperature increments of 20 °C and selected relative humidity levels of 20%, 50%, 80%, and 100%. Although C11 demonstrates the most favorable balance between electrochemical performance, membrane hydration, oxygen transport, and spatial uniformity among the evaluated conditions, additional simulations with finer temperature and humidity increments around this operating point would be necessary to identify the precise optimum and assess its sensitivity to operating conditions.

Overall, the results demonstrate that PEMFC response to climate-related environmental stress is governed by the coupled interaction of temperature, relative humidity, electrochemical loading, water transport, reactant availability, and thermal management rather than by any individual parameter. The multiphysics analysis revealed two fundamentally different limiting regimes. Hot–dry conditions intensified membrane dehydration, increased ionic resistance, reduced the sustainable current-density range, and ultimately deteriorated net power production. Conversely, highly humid conditions improved membrane hydration but progressively introduced liquid-water accumulation, oxygen-transport resistance, pressure-drop penalties, and additional auxiliary-energy requirements. The transition between these regimes confirms that increasing either temperature or humidification cannot independently guarantee improved performance and that environmental resilience instead depends on maintaining an appropriate balance between membrane hydration and effective reactant transport.

Among the investigated environmental scenarios, the intermediate-temperature and moderately high-humidity region consistently provided the most favorable compromise between the competing transport mechanisms. In particular, the behavior around 60 °C and 80% RH (C11) was characterized by favorable membrane hydration, comparatively uniform internal transport, strong oxygen utilization, reduced transport penalties, and the largest admissible operating-current envelope. The integrated system-level assessment further demonstrated that these internal improvements translate into meaningful practical benefits through enhanced net power output and energy-conversion performance. In contrast, the hot–dry condition represented the most severe operating environment, illustrating how simultaneous thermal and humidity extremes can amplify rather than simply add their individual effects.

Taken collectively, these findings establish a direct connection between climate exposure, internal multiphysics processes, and usable PEMFC system performance. More importantly, the results indicate that environmental resilience should not be defined solely by the ability of a fuel cell to continue operating under extreme conditions, but by its capacity to maintain stable hydration, effective mass transport, acceptable thermal behavior, and useful power output without excessive auxiliary or efficiency penalties. The identified operating envelopes and dominant degradation mechanisms therefore provide a physically grounded basis for climate-adaptive control strategies, improved thermal and water-management systems, and the design of PEMFC power systems capable of reliable operation under increasingly variable environmental conditions.

4. Conclusions

This study investigated the environmental resilience of PEM fuel cells under coupled temperature and relative-humidity extremes through a three-dimensional, steady-state, non-isothermal multiphysics framework. Sixteen environmental scenarios covering temperatures from 20 to 80 °C and relative humidities from 20 to 100% were examined while maintaining the remaining geometrical and operating parameters constant. By simultaneously resolving electrochemical performance, membrane hydration, oxygen

transport, liquid-water behavior, thermal response, current-density uniformity, pressure losses, and system-level performance, the analysis demonstrates that PEMFC response to environmental stress cannot be adequately interpreted through polarization characteristics or any single operating variable alone.

Two fundamentally different environmental limitation regimes were identified. Under hot–dry conditions, insufficient membrane hydration becomes the dominant constraint, reducing proton conductivity and increasing ohmic losses while producing stronger spatial electrochemical and thermal non-uniformities. The hot–dry C13 scenario represents the most severe manifestation of this mechanism, with current-density non-uniformity reaching approximately 21.2% and temperature non-uniformity approximately 5.4 K, compared with only 7.4% and 2.2 K, respectively, under C11. At the opposite extreme, increasing humidity improves membrane hydration but eventually shifts the dominant limitation toward liquid-water accumulation and restricted oxygen transport. The results therefore reveal a transition from dehydration-controlled to water-management and mass-transfer-controlled operation rather than a monotonic benefit from increasing either temperature or humidity.

A distinct environmentally resilient operating region was consequently identified around 60 °C and 80% RH. The C11 condition provides a membrane water content of approximately 14.3 while maintaining a minimum cathode oxygen concentration of approximately 4.6 mol m^{-3} and comparatively limited liquid-water saturation. This balance is further reflected in an oxygen utilization of approximately 79.4%, the highest among the investigated scenarios. More importantly, the favorable internal transport state translates directly into an expanded operating envelope: C11 sustains an admissible current density of approximately 1.98 A cm^{-2}, whereas the hot–dry C13 condition is restricted to only 0.74 A cm^{-2}. This substantial difference demonstrates that environmental resilience has direct implications for the usable loading capability of PEMFC systems rather than representing only a secondary variation in cell performance.

The analysis also demonstrates that climate-induced environmental stresses propagate beyond the membrane–electrode assembly to affect auxiliary and system-level performance. Increasing humidity raises cathode pressure drop and pumping requirements, particularly under lower-temperature saturated conditions, illustrating that improved hydration may impose an auxiliary-energy penalty when water removal becomes inadequate. At the system level, C11 achieves the highest reported net power density of approximately 1.04 W cm^{-2}, whereas C13 decreases to approximately 0.49 W cm^{-2}. The integrated assessment similarly identifies C11 as the most favorable condition in terms of thermal efficiency and specific carbon intensity, with the latter reaching approximately 12.5 g CO_2 kWh^{-1} compared with approximately 27.4 g CO_2 kWh^{-1} for C13 under the assumptions adopted in the study. These findings establish an important connection between microscale transport phenomena, usable electrical output, auxiliary-energy consumption, and the broader sustainability performance of hydrogen power systems.

The principal implication of this work is therefore that environmental resilience in PEMFCs should be defined as the ability to preserve a balanced multiphysics operating state, rather than merely maintaining electrical generation during environmental extremes. Effective resilience requires simultaneous preservation of membrane hydration, oxygen accessibility, thermal and current-density uniformity, water removal, and acceptable auxiliary-energy demand. The identified temperature–humidity operating envelope provides a physics-based foundation for adaptive humidification, cooling, reactant-flow, and load-management strategies capable of responding to changing climatic conditions. Future work should extend the present steady-state framework toward transient climatic disturbances, experimentally validated environmental cycling,

degradation-aware simulations, and dynamic control strategies to determine whether the resilient operating windows identified here can also minimize long-term material degradation and performance loss under realistic climate exposure.

Author Contributions: Conceptualization, S.S.A. and M.R.A.; methodology, S.S.A. and A.M.S.; software, S.S.A. and A.E.Z.; validation, M.R.A. and A.M.S.; formal analysis, S.S.A. and A.E.Z.; investigation, S.S.A., M.R.A. and A.M.S.; resources, A.E.Z. and N.K.; data curation, A.M.S. and N.K.; writing—original draft preparation, S.S.A.; writing—review and editing, S.S.A., M.R.A., A.M.S., A.E.Z. and N.K.; visualization, A.M.S. and A.E.Z.; supervision, S.S.A.; project administration, S.S.A. and M.R.A. All authors have read and agreed to the published version of the manuscript.

Funding: This research received no external funding.

Data Availability Statement: The data supporting the findings of this study are available from the corresponding author upon reasonable request.

Conflicts of Interest: The authors declare no conflicts of interest.

Nomenclature

Symbol	Description	Unit
a	Water activity	–
C_P	Specific heat capacity	J kg^{-1} K^{-1}
CO_2	Local oxygen concentration	mol m^{-3}
CO_2,in	Oxygen concentration at cathode inlet	mol m^{-3}
CO_2,min	Minimum local oxygen concentration	mol m^{-3}
CO_2,ref	Reference oxygen concentration	mol m^{-3}
c f	Concentration of fixed ionic sites in the membrane	mol m^{-3}
CVj	Coefficient of variation in local current density	–
CVj,norm	Normalized current density nonuniformity	–
Di	Bulk diffusion coefficient of species i	m^2 s^{-1}
Di,eff	Effective diffusion coefficient of species i in porous media	m^2 s^{-1}
Dw	Water diffusion coefficient in the membrane	m^2 s^{-1}
E^0	Standard equilibrium potential	V
Eeq	Equilibrium potential	V
Erev	Reversible cell potential	V
ERI	Environmental Resilience Index	–
F	Faraday constant	C mol^{-1}
Hch	Flow-channel height	m
j	Local current density	A m^{-2}
j_0	Exchange current density	A m^{-2}
javg	Spatially averaged current density	A m^{-2}
K	Permeability of porous medium	m^2
keff	Effective thermal conductivity	W m^{-1} K^{-1}
Lch	Flow-channel length	m
N	Number of experimental data points	–
NH_2	Hydrogen molar consumption flux	mol m^{-2} s^{-1}
NO_2	Oxygen molar consumption flux	mol m^{-2} s^{-1}
NH_2O	Water production flux	mol m^{-2} s^{-1}
Nw	Net water flux through the membrane	mol m^{-2} s^{-1}
nd	Electro-osmotic drag coefficient	–
nH_2O	Number or amount of water molecules in the membrane	–
nSO_3^-	Number or amount of sulfonic-acid groups	–
P	Power density	W m^{-2}
Pref	Power density under reference environmental condition	W m^{-2}
p	Pressure	Pa

pH_2	Hydrogen partial pressure	Pa
pO_2	Oxygen partial pressure	Pa
pH_2O	Water-vapor partial pressure	Pa
pin	Total inlet pressure	Pa
Psat	Saturation vapor pressure of water	Pa
Qact	Heat generation associated with activation losses	W m^{-3}
Qgen	Total volumetric heat generation	W m^{-3}
Qohm	Ohmic heat generation	W m^{-3}
Qrev	Reversible entropic heat generation	W m^{-3}
R	Universal gas constant	J mol^{-1} K^{-1}
RH	Relative humidity	– or %
RO_2	Oxygen-transport resilience indicator	–
RP	Power-density retention ratio	–
RV	Voltage retention ratio	–
Rλ	Membrane hydration retention ratio	–
Si	Source or sink term for species i	kg m^{-3} s^{-1} or mol m^{-3} s^{-1}
Sj	Electrochemical current source term	A m^{-3}
Sm	Mass source or sink term	kg m^{-3} s^{-1}
ST	Volumetric energy source term	W m^{-3}
Su	Momentum source term	N m^{-3}
Sl,avg	Volume-averaged liquid-water saturation	–
sl	Local liquid-water saturation	–
T	Local absolute temperature	K
Tmax	Maximum temperature in the computational domain	K
Tmin	Minimum temperature in the computational domain	K
u	Velocity vector	m s^{-1}
V	Cell voltage	V
Vexp	Experimentally measured cell voltage	V
Vp	Volume of the investigated porous region	m^3
Vref	Cell voltage under the reference environmental condition	V
Vsim	Numerically predicted cell voltage	V
Wch	Flow-channel width	m
w_1–w_5	Weighting factors used in the Environmental Resilience Index	–
x H_2O	Water-vapor mole fraction	–
Y i	Mass fraction of species i	–
α a	Anodic charge-transfer coefficient	–
α c	Cathodic charge-transfer coefficient	–
γ	Oxygen concentration exponent	–
δCL	Catalyst-layer thickness	m
δGDL	Gas-diffusion-layer thickness	m
δmem	Membrane thickness	m
ΔT	Temperature difference between maximum and minimum cell temperatures	K
ε	Porosity	–
εCL	Catalyst-layer porosity	–
εGDL	Gas-diffusion-layer porosity	–
η	Activation overpotential	V
λ	Membrane water content	mol H_2O mol^{-1} SO_3^-
λavg	Spatially averaged membrane water content	mol H_2O mol^{-1} SO_3^-
λavg,ref	Average membrane water content under reference condition	mol H_2O mol^{-1} SO_3^-
μ	Dynamic viscosity	Pa s
ρ	Gas-mixture density	kg m^{-3}
σ	Electrical or ionic conductivity	S m^{-1}
σ j	Standard deviation of local current density	A m^{-2}
σ m	Protonic conductivity of the membrane	S m^{-1}

https://doi.org/10.3390/cleantechnol8060188

σ s	Electronic conductivity of the solid phase	S m^{-1}
φ m	Membrane-phase electric potential	V
φ s	Solid-phase electric potential	V

Abbreviations

Abbreviation	Meaning
CL	Catalyst Layer
GDL	Gas Diffusion Layer
HEF	Journal of Human, Earth, and Future
MAPE	Mean Absolute Percentage Error
MEA	Membrane–Electrode Assembly
PEMFC	Proton Exchange Membrane Fuel Cell
RH	Relative Humidity
RMSE	Root-Mean-Square Error

References

1. Bernardi, M.; Tangorra, R.R.; Palmisano, P.; Bogliano, A. Chemicals From Renewable Sources. In *Reference Module in Chemistry, Molecular Sciences and Chemical Engineering*; Elsevier: Amsterdam, The Netherlands, 2016.
2. Blunt, M.J.; Lin, Q. Flow in Porous Media in the Energy Transition. *Engineering* **2022**, *14*, 10–14. https://doi.org/10.1016/j.eng.2021.08.008.
3. Essoufi, M.; Benzaouia, M.; Hajji, B.; Rabhi, A.; Calí, M. Adaptive frequency separation-based energy management strategy using fuzzy logic for fuel cell-battery hybrid vehicles. *Results Eng.* **2026**, *29*, 109554. https://doi.org/10.1016/j.rineng.2026.109554.
4. Kang, H.; Kim, S.E.; Park, J.C. Development of a fuel cell Energy-Economics evaluation model for Distributed energy Promotion: Focusing on Establishing hydrogen city Policies in Seoull. *Energy Convers. Manag. X* **2026**, *30*, 101679. https://doi.org/10.1016/j.ecmx.2026.101679.
5. Babay, M.-A.; Adar, M.; El Messoussi, M.E.; Chebak, A.; Mabrouki, M. Three-Dimensional Non-Isothermal CFD investigation of proton exchange membrane fuel Cells: Coupled Thermal–Electrochemical analysis and performance evaluation. *Fuel* **2026**, *409*, 137823. https://doi.org/10.1016/j.fuel.2025.137823.
6. Bakır, H.; Ağbulut, Ü. Efficient design, operation and control of commercial proton exchange membrane fuel cells (PEMFCs) in clean energy technology. *Int. J. Hydrogen Energy* **2026**, *197*, 152498. https://doi.org/10.1016/j.ijhydene.2025.152498.
7. Hu, T.; Yang, Z.; Zheng, W.; Li, H.; Liu, W.; Zhu, Q. Performance enhancement through integrated design of assembly pressure and porosity of gas diffusion layer for HT-PEMFC based on coupled electrochemical–thermal–mechanical modeling. *Energy Convers. Manag.* **2026**, *350*, 120939. https://doi.org/10.1016/j.enconman.2025.120939.
8. Maiket, Y.; Yeetsorn, R.; Hissel, D. Grid-independent electric vehicle battery charging using a direct-current PEMFC-SC hybrid system. *J. Power Sources* **2026**, *662*, 238707. https://doi.org/10.1016/j.jpowsour.2025.238707.
9. Tian, Z.; Huangfu, Y.; Al-Durra, A.; Muyeen, S.; Zhou, D. Accurate and efficient parameter identification of fuel cells using tree seed algorithm based on adaptive differential evolution and Dempster-Shafer evidence theory. *Renew. Energy* **2026**, *260*, 125198. https://doi.org/10.1016/j.renene.2026.125198.
10. Yu, B.; Jia, X.; Han, T.; Li, J.; Xu, L.; Fang, C.; Zhang, L.; Meng, D.; Hu, Z.; Ouyang, M. Modeling and degradation-aware energy management strategy for fuel cell vehicle considering cathode catalyst layer status. *J. Power Sources* **2026**, *668*, 239228. https://doi.org/10.1016/j.jpowsour.2025.239228.
11. Zhang, B.-X.; Wang, H.-Q.; Wang, L.-Q.; Zhu, K.-Q.; Wang, Y.-B.; Wang, S.-Y.; Yang, Y.-R.; Wang, X.-D. Comprehensive impact of the thermal contact resistance between various components of a PEMFC with a deformed MEA on performance. *Int. Commun. Heat Mass Transf.* **2026**, *172*, 110633. https://doi.org/10.1016/j.icheatmasstransfer.2026.110633.
12. Al-Falahat, A.; Alrwashdeh, S.S. Mechanistic and optimization based analysis of bio inspired multiscale flow fields for water management in PEM fuel cells. *Int. J. Electrochem. Sci.* **2026**, *21*, 101398. https://doi.org/10.1016/j.ijoes.2026.101398.
13. Liu, C.; Lin, Q.; Zhang, J.; Liu, Q.; Wan, X.; Bi, W. Single-walled carbon Nanotube-Encapsulated polyoxometalates for Wide-Range humidity PEM fuel cells. *Fuel* **2026**, *418*, 138688. https://doi.org/10.1016/j.fuel.2026.138688.
14. Lv, B.; Pan, C. Research on optimization of PEMFC stack compression pressure based on mechanical-electrochemical coupling model. *Fuel* **2026**, *412*, 138078. https://doi.org/10.1016/j.fuel.2025.138078.

15. Parmar, A.; Aljaidi, M.; Maheshwari, S.; Arpita; Jangir, P.; Jangid, R.; Kumar, S.; Kumar, G.; Rani, R.; Khishe, M. High accuracy parameter estimation of solid oxide fuel cells using a surrogate assisted differential evolution with multi sampling mechanism. *Electrochem. Commun.* **2025**, *180*, 108060. https://doi.org/10.1016/j.elecom.2025.108060.
16. Qin, H.; Yan, F.; Feng, S.; Su, Y.; Li, X. Design and optimization of a depth-graded trapezoidal baffle flow channel for PEMFC based on genetic algorithm. *Fuel* **2026**, *413*, 138238. https://doi.org/10.1016/j.fuel.2025.138238.
17. Singla, M.K.; Ali, S.A.M.; Kumar, R.; Jangir, P.; Khishe, M.; Gulothungan, G.; Mahmoud, H.A. Revolutionizing proton exchange membrane fuel cell modeling through hybrid aquila optimizer and arithmetic algorithm optimization. *Sci. Rep.* **2025**, *15*, 5122. https://doi.org/10.1038/s41598-025-89631-8.
18. Babay, M.-A.; Adar, M.; Chebak, A.; Mabrouki, M. Exploring the sustainability of serpentine flow-field fuel cell, straight channel PEM fuel cells hight temperature through numerical analysis. *Energy Nexus* **2024**, *14*, 100283. https://doi.org/10.1016/j.nexus.2024.100283.
19. Chen, M.; Dong, W.; Chen, Q.; Wang, L.; Wang, Y.; Wu, C.; Wang, X.; Xia, C.; Wang, H.; Wang, B. K doped LiNi0.8Co0.15Al0.05O2-δ electrode for solid oxide fuel cells operating at low temperatures down to 350 °C. *Chem. Eng. J.* **2024**, *502*, 158034. https://doi.org/10.1016/j.cej.2024.158034.
20. Gasteiger, H.; Panels, J.; Yan, S. Dependence of PEM fuel cell performance on catalyst loading. *J. Power Sources* **2004**, *127*, 162–171. https://doi.org/10.1016/j.jpowsour.2003.09.013.
21. Khan, R.; Rasheed, R.H.; Ghodratallah, P.; Singh, N.S.S.; Hussein, S.A.; Rajab, H.; Hajlaoui, K.; Dixit, S. Multi-objective optimization of a biomass-fueled hybrid system integrating PEM fuel cell with ammonia-water cooling cycle aiming at clean multi-energy generation. *Int. J. Hydrogen Energy* **2025**, *195*, 152287. https://doi.org/10.1016/j.ijhydene.2025.152287.
22. Wang, S.; Hu, X.; Zhou, Z.; Wang, Q.; Ye, K.; Sui, S.; Hu, M.; Jiang, F. Critical performance comparisons between the high temperature and the low temperature proton exchange membrane fuel cells. *Sustain. Energy Technol. Assess.* **2023**, *60*, 103529. https://doi.org/10.1016/j.seta.2023.103529.
23. Kim, S.; Lee, H.; Kim, C.; Jang, I.; Lee, K.; Sun, S.; Lee, D.; Kim, J.; Park, K.; Lee, G.; et al. Interface-reinforcing sintering step for highly stable operation of proton-conducting fuel cell stack. *J. Power Sources* **2022**, *548*, 232082. https://doi.org/10.1016/j.jpowsour.2022.232082.
24. Li, S.; Sang, X.; Zhu, Z.; Jiang, W.; Wang, W.; Li, C.; Wang, X. Parametric analysis and energy efficiency optimization control of integrated thermal management system with waste heat utilization for fuel cell vehicles. *Int. J. Hydrogen Energy* **2026**, *204*, 153037. https://doi.org/10.1016/j.ijhydene.2025.153037.
25. Park, S.; Kim, M.-H.; Um, S. Phase separation modeling of water transport in polymer electrolyte membrane fuel cells using the Multiple-Relaxation-Time lattice Boltzmann method. *Chem. Eng. J.* **2024**, *495*, 153629. https://doi.org/10.1016/j.cej.2024.153629.
26. Hottinen, T.; Himanen, O. PEMFC temperature distribution caused by inhomogeneous compression of GDL. *Electrochem. Commun.* **2007**, *9*, 1047–1052. https://doi.org/10.1016/j.elecom.2006.12.018.
27. Kim, S.S.; Hong, S.C. Response regarding Konsolakis's comments on "Effect of CeO_2 addition to Rh/Al_2O_3 catalyst on N_2O decomposition" by S.S. Kim, S.J. Lee, S.C. Hong in Chem. Eng. J. 169 (2011) 173. *Chem. Eng. J.* **2012**, *183*, 552. https://doi.org/10.1016/j.cej.2011.11.106.
28. Saleh, R.; Memarzadeh, A.; Hurdoganoglu, D.; Sahmani, S.; Jen, T.-C.; Safaei, B. A comprehensive review on atomic layer deposition on key components in fuel cells. *Fuel* **2025**, *395*, 135172. https://doi.org/10.1016/j.fuel.2025.135172.
29. Göbel, M.; Kirsch, S.; Schwarze, L.; Schmidt, L.; Scholz, H.; Haußmann, J.; Klages, M.; Scholta, J.; Markötter, H.; Alrwashdeh, S.; et al. Transient limiting current measurements for characterization of gas diffusion layers. *J. Power Sources* **2018**, *402*, 237–245. https://doi.org/10.1016/j.jpowsour.2018.09.003.
30. Markötter, H.; Manke, I.; Böll, J.; Alrwashdeh, S.; Hilger, A.; Klages, M.; Haussmann, J.; Scholta, J. Morphology correction technique for tomographic in-situ and operando studies in energy research. *J. Power Sources* **2019**, *414*, 8–12. https://doi.org/10.1016/j.jpowsour.2018.12.072.
31. Al-Falahat, A.; Kardjilov, N.; Khanh, T.; Markötter, H.; Boin, M.; Woracek, R.; Salvemini, F.; Grazzi, F.; Hilger, A.; Alrwashdeh, S.; et al. Energy-selective neutron imaging by exploiting wavelength gradients of double crystal monochromators—Simulations and experiments. *Nucl. Instrum. Methods Phys. Res. Sect. A Accel. Spectrometers Detect. Assoc. Equip.* **2019**, *943*, 162477. https://doi.org/10.1016/j.nima.2019.162477.
32. Alrwashdeh, S.S. The effect of solar tower height on its energy output at Ma'an-Jordan. *AIMS Energy* **2018**, *6*, 959–966. https://doi.org/10.3934/ENERGY.2018.6.959.
33. Alrwashdeh, S.S. Energy profit evaluation of a photovoltaic system from a selected building in Jordan. *Results Eng.* **2023**, *18*, 101177. https://doi.org/10.1016/j.rineng.2023.101177.

34. Gostick, J.T.; Ioannidis, M.A.; Fowler, M.W.; Pritzker, M.D. Wettability and capillary behavior of fibrous gas diffusion media for polymer electrolyte membrane fuel cells. *J. Power Sources* **2009**, *194*, 433–444. https://doi.org/10.1016/j.jpowsour.2009.04.052.
35. Hasan, N.; Ishraque, F.; Shezan, S.A.; Kamwa, I.; Ahmad, K.; Alrwaili, A.; Alruwaili, M.; Amin, N.; Ahmad, N. Hydrogen and fuel cells as the cornerstones of the universal energy transfer—A comprehensive review. *Int. J. Hydrogen Energy* **2026**, *209*, 153486. https://doi.org/10.1016/j.ijhydene.2026.153486.
36. Jangir, P.; Ezugwu, A.E.; Arpita; Agrawal, S.P.; Pandya, S.B.; Parmar, A.; Gulothungan, G.; Abualigah, L. Precision parameter estimation in Proton Exchange Membrane Fuel Cells using depth information enhanced Differential Evolution. *Sci. Rep.* **2024**, *14*, 29591. https://doi.org/10.1038/s41598-024-81160-0.
37. Owejan, J.; Goebel, S. Performance evaluation of porous gas channel ribs in a polymer electrolyte fuel cell. *J. Power Sources* **2021**, *494*, 229740. https://doi.org/10.1016/j.jpowsour.2021.229740.
38. Pasaogullari, U.; Wang, C.-Y. Two-phase transport and the role of micro-porous layer in polymer electrolyte fuel cells. *Electrochim. Acta* **2004**, *49*, 4359–4369. https://doi.org/10.1016/j.electacta.2004.04.027.
39. Qin, H.; Yan, F.; Feng, S.; Su, Y.; Li, X. Design and optimization of a biomimetic lymphatic valve baffle flow channel for PEMFC based on a genetic algorithm. *Int. Commun. Heat Mass Transf.* **2026**, *173*, 110761. https://doi.org/10.1016/j.icheatmasstransfer.2026.110761.
40. Springer, T.E.; Zawodzinski, T.A.; Gottesfeld, S. Polymer Electrolyte Fuel Cell Model. *J. Electrochem. Soc.* **1991**, *138*, 2334. https://doi.org/10.1149/1.2085971.
41. Tien, N.N.; Van, H.N.; Duy, V.N.; Trinh, H.P. Simulation-based comparative analysis of different chassis configurations of hybrid fuel cell vehicle. *Int. J. Thermofluids* **2024**, *24*, 100968. https://doi.org/10.1016/j.ijft.2024.100968.
42. Weber, S.; Prifling, B.; Jeela, R.K.; Prahs, A.; Schneider, D.; Nestler, B.; Schmidt, V. A time-continuous approach to analyzing anode aging in solid-oxide fuel cells via stochastic 3D microstructure modeling and physics-based simulations. *Comput. Mater. Sci.* **2026**, *264*, 114491. https://doi.org/10.1016/j.commatsci.2026.114491.
43. Zhang, Y.; Peng, Y.; Wan, Q.; Ye, D.; Wang, A.; Zhang, L.; Jiang, W.; Liu, Y.; Li, J.; Zhuang, X.; et al. Fuel cell power source based on decaborane with high energy density and low crossover. *Mater. Today Energy* **2023**, *32*, 101244. https://doi.org/10.1016/j.mtener.2022.101244.
44. Zuo, Q.; Wang, G.; Shen, Z.; Zhu, X.; Xie, Y.; Li, Y.; Ma, Y.; Zhang, H. Digital twinning of multi-physics field performance of faceted novel snake coil flow field proton exchange membrane fuel cells. *J. Power Sources* **2025**, *649*, 237442. https://doi.org/10.1016/j.jpowsour.2025.237442.

Disclaimer/Publisher's Note: The statements, opinions and data contained in all publications are solely those of the individual author(s) and contributor(s) and not of MDPI and/or the editor(s). MDPI and/or the editor(s) disclaim responsibility for any injury to people or property resulting from any ideas, methods, instructions or products referred to in the content.